IJMMM International Journal of Minerals, Metallurgy and Materials 矿物冶金与材料学报（英文版）

Multifunctional applications of barium zinc vanadate nanoparticles for photocatalytic dye degradation, energy storage and sensing applications

S. Ishwarya, H.P. Nagaswarupa, Yashwanth Venkatraman Naik, Basavaraju N, Ramachandra Naik, Abdullah N. Alodhayb, Saravanan Pandiaraj, Burragoni Sravanthi Goud, and Jae Hong Kim

Cite this article as:
S. Ishwarya, H.P. Nagaswarupa, Yashwanth Venkatraman Naik, Basavaraju N, Ramachandra Naik, Abdullah N. Alodhayb, Saravanan Pandiaraj, Burragoni Sravanthi Goud, and Jae Hong Kim, Multifunctional applications of barium zinc vanadate nanoparticles for photocatalytic dye degradation, energy storage and sensing applications, *Int. J. Miner. Metall. Mater.*, 32(2025), No. 12, pp. 3052-3071. https://doi.org/10.1007/s12613-025-3160-4

View the article online at SpringerLink or IJMMM Webpage.

Articles you may be interested in

Yan Liu, Kaiyang Guo, Yuanmeng Ge, Wenzheng Yan, Kai Gu, Yapeng Tian, and Xinwei Cui, Structural engineering of MXenes towards high electrochemical performance in supercapacitors, *Int. J. Miner. Metall. Mater.*, 32(2025), No. 8, pp. 1783-1812. https://doi.org/10.1007/s12613-025-3146-2

Choulong Veann, Thongsuk Sichumsaeng, Ornuma Kalawa, Narong Chanlek, Pinit Kidkhunthod, and Santi Maensiri, Structure and electrochemical performance of delafossite $AgFeO_2$ nanoparticles for supercapacitor electrodes, *Int. J. Miner. Metall. Mater.*, 32(2025), No. 1, pp. 201-213. https://doi.org/10.1007/s12613-024-2992-7

Xing-hua Qin, Ye-hong Du, Peng-chao Zhang, Xin-yu Wang, Qiong-qiong Lu, Ai-kai Yang, and Jun-cai Sun, Layered barium vanadate nanobelts for high-performance aqueous zinc-ion batteries, *Int. J. Miner. Metall. Mater.*, 28(2021), No. 10, pp. 1684-1692. https://doi.org/10.1007/s12613-021-2312-4

Xin Yu, Congcong Li, Jian Zhang, Lili Zhao, Jinbo Pang, and Longhua Ding, Recent progress on Sn_3O_4 nanomaterials for photocatalytic applications, *Int. J. Miner. Metall. Mater.*, 31(2024), No. 2, pp. 231-244. https://doi.org/10.1007/s12613-023-2761-z

Yang Xue, Xiaoming Liu, Na Zhang, Yang Shao, and Chunbao(Charles) Xu, Enhanced photocatalytic performance of iron oxides@HTCC fabricated from zinc extraction tailings for methylene blue degradation: Investigation of the photocatalytic mechanism, *Int. J. Miner. Metall. Mater.*, 30(2023), No. 12, pp. 2364-2374. https://doi.org/10.1007/s12613-023-2723-5

Junjie Zhang and Xiang Wu, Dual-ion carrier storage through Mg^{2+} addition for high-energy and long-life zinc-ion hybrid capacitor, *Int. J. Miner. Metall. Mater.*, 31(2024), No. 1, pp. 179-185. https://doi.org/10.1007/s12613-023-2724-4

IJMMM WeChat

QQ author group

INTERNATIONAL JOURNAL OF
Minerals, Metallurgy and Materials

Volume 32, Number 12, December 2025
Page 3052

Research Article https://doi.org/10.1007/s12613-025-3160-4

Multifunctional applications of barium zinc vanadate nanoparticles for photocatalytic dye degradation, energy storage and sensing applications

S. Ishwarya[1)], *H.P. Nagaswarupa*[1),✉], *Yashwanth Venkatraman Naik*[2)], *Basavaraju N*[3)], *Ramachandra Naik*[4),✉], *Abdullah N. Alodhayb*[5)], *Saravanan Pandiaraj*[6)], *Burragoni Sravanthi Goud*[7),✉], *and Jae Hong Kim*[7),✉]

1) Department of Studies in Chemistry, Shivagangothri, Davangere University, Davanagere 577007, India
2) Department of Physics, RV Institute of Technology and Management, Bangalore 560076, India
3) Research Center, Department of Science, East West Institute of Technology, Bangalore 560091, India
4) Department of Physics, New Horizon College of Engineering, Bangalore 560103, India
5) Research Chair for Tribology, Surface, and Interface Sciences, Department of Physics and Astronomy, College of Science, King Saud University, Riyadh 11451, Saudi Arabia
6) Department of Self-development skills, King Saud University, Riyadh 11451, Saudi Arabia
7) Department of Chemical Engineering, Yeungnam University, Gyeongbuk 38541, Republic of Korea
(Received: 24 February 2025; revised: 11 April 2025; accepted: 16 April 2025)

Abstract: The multifunctional characteristics of barium zinc vanadate ($BaZnV_2O_7$) nanoparticles (BZV NPs) were explored in this study, focusing on their photocatalytic activity, supercapacitor performance, and sensing abilities. X-ray diffraction analysis confirmed that the crystallites were 40.3 nm in size, whereas ultraviolet visible diffuse reflectance spectroscopy revealed an energy bandgap of 5.28 eV. Functional groups, elemental composition, and morphology were assessed using Fourier transform infrared spectroscopy, energy-dispersive X-ray spectroscopy, and scanning electron microscopy, respectively. The photocatalytic efficiency of the BZV NPs was evaluated at various catalyst dosages, dye concentrations, and pH levels, for the degradation of acid black-52 (AB-52) dye under UV light. Cyclic voltammetry and galvanostatic charge-discharge analyses were performed to determine the energy storage and cyclic stability of the BZV-NP-modified carbon paste electrode. In addition, a novel electrochemical sensor based on BZV was developed to accurately detect the concentration of biomolecules and chemical drugs. BZV nanoparticles exhibited remarkable photocatalytic dye degradation up to 80.4%, indicating their application in waste water treatment. The BZV-NP-modified carbon paste electrode exhibited a superior specific capacitance of 714.15 $F \cdot g^{-1}$ with excellent cycling stability over 1000 cycles. The electrodes efficiently detected biomolecules such as ascorbic acid and uric acid, chemical drugs including paracetamol and ibuprofen, and heavy metals such as mercury, cobalt, and cadmium in the concentration range of 1–5 mM. The limit of detection (LOD) was measured for all analytes, and the electrode exhibited high sensitivity. These multifunctional properties render BZV promising material for energy storage and environmental monitoring applications.

Keywords: barium zinc vanadate; acid black-52; photocatalytic activity; supercapacitor; sensor; limit of detection.

1. Introduction

Commercial procedures have resulted in the widespread use of hazardous chemicals, which are used in various ways. This has led to environmental pollution and adversely affected human health globally, especially with recent rapid industrialization and upgradation [1]. The discharge of various hazardous organic pollutants from industrial effluents continuously contaminates water supplies. The most important contaminants present in effluents are colorants and dyes, which are extensively used worldwide, especially in the printing, leather, and apparel industries. According to the World Bank, the processing and dyeing of clothing and textiles is responsible for one-fifth of the world's industrial water pollution [2]. The primary ingredients in textile effluents include cationic and anionic dyes, such as acid black-52 (AB-52), rhodamine B (RhB), methylene blue (MB), Congo red (CR), and acid red-88 (AR-88). These dyes have detrimental and necrotic effects on human health [3], other living organisms, and the environment because they are nondegradable, poisonous, persistent, and drastically reduce water quality, even in extremely low quantities. Thus, there has been wide-

✉ Corresponding authors: H.P. Nagaswarupa E-mail: nagaswarupa77@gmail.com;
Ramachandra Naik E-mail: rcnaikphysics@gmail.com;
Burragoni Sravanthi Goud E-mail: sravsdb.18@gmail.com;
Jae Hong Kim E-mail: jaehkim@ynu.ac.kr

Springer

spread deterioration in the quality of drinkable water [4]. Numerous advanced techniques and strategies have been investigated to eliminate these poisonous chemical dyes and dangerous pollutants from aquatic environments, including membrane filtration, ozonation, adsorption, chemical oxidation, and biodegradation [5–7]. However, these methods are expensive, have limited applicability, and result in secondary pollutants. In contrast, photocatalysis is recognized as a promising, versatile, stable, low-energy-consuming, and highly effective advanced oxidation technique that uses sunlight supported by a catalyst to completely decompose hazardous dyes into CO_2 and H_2O in an environmentally friendly manner, without byproduct formation [8–9]. The primary goal of this study was to create photocatalytic materials with an enhanced oxidation process that is low-cost, highly efficient, and effective for wastewater treatment. Metal/metal oxides (such as vanadates), metal composites, nitrides, and sulfides have recently garnered much interest among the semiconductor-based catalysts employed for dye degradation. This is primarily due to their environmentally friendly wastewater treatment applications [10].

Because of their exceptional qualities such as low toxicity, abundance, and affordable synthesis techniques, vanadates are an excellent choice among metal oxides as catalysts for the degradation of AB-52 [11]. The removal of photogenerated electrons and the rearrangement of electron-hole pairs are significantly affected by the molecular oxygen absorption capacity of vanadate nanoparticles (NPs). Thus, the chemical events leading to the breakdown and transformation of pollutants can be driven by ultraviolet radiation. Barium zinc vanadate ($BaZnV_2O_7$) nanoparticles (BZV NPs) can be produced for various uses using a simple chemical combustion procedure, among many other synthesis methods. The benefits of this method include relatively low toxicity, quick scaling for larger production, homogeneity, extensibility, low cost, high yield, versatility, controlled particle size, and compatibility with a range of materials [12]. To achieve superior degradation performance, a few parameters related to photocatalyst efficiency must be addressed. Some of the variables that influence the photocatalytic activity are the surface arrangement, bandgap energy, size and morphology, surface area, crystallinity, and light-harvesting efficiency [13]. Therefore, the development of high-performance photocatalysts is essential for the efficient breakdown of organic dyes in wastewater. Boosting the absorption of visible light, regulating pH, maintaining catalyst stability, understanding complex reaction kinetics, and sustainability and applicability of dye removal using photocatalytic methods are some of the major obstacles that arise during photocatalytic dye degradation [14]. To address these problems, starting with ensuring sufficient photoelectron production, considerable efforts have been made to modify the structural characteristics and improve the process parameters. The pH of the solution affects the surface charges of both the dye molecules and photocatalyst, which in turn affects how the dye molecules interact and adsorb [15]. It is important to consider how pH affects the surface charge and reactivity of nanoparticles. By modifying the pH, the electrostatic interactions between AB-52 and BZV NPs can be altered, which, in turn, affects the degradation efficiency. Furthermore, photoelectrons appear only when there is enough catalyst present and when the catalyst absorbs light. A significant factor influencing the availability of catalytic reaction active sites and, consequently, the degradation rate is the amount of BZV NPs. Up to a certain point, more catalyst aids the formation of more photoelectrons; after that, the shielding effect begins to obstruct light absorption, which reduces the generation of photoelectrons. Furthermore, hydroxyl radicals aid in the breakdown of dye molecules, and oxygen serves as an electron acceptor in photocatalytic redox reactions. The effects of reactive species and oxygen in solution are also significant [16–17].

Supercapacitors have been identified as conceivably beneficial energy storage devices because of their higher performance, longer cycle stability, and reduced maintenance costs. In addition, supercapacitors offer far higher energy densities than traditional dielectric capacitors, longer life cycles, and higher power densities than batteries [18–26]. The three different forms of energy storage mechanisms that are affected by the charges stored at the electrode-electrolyte interface are hybrid capacitors, electric double-layer capacitors (EDLCs), and pseudocapacitors. Pseudocapacitors accelerate the redox process by transferring charges across the electrode and electrolyte surfaces. The core requirement of a supercapacitor for high power density is the utilization of redox reactions of electrolyte ions in electrode materials [27–29]. Transition-metal oxides (ZnO, RuO_2, NiO, MnO_2, Co_3O_4, CuO, and Fe_2O_3), carbon-based materials (graphene, carbon spheres, and carbon nanotubes), and conducting polymers are used as electrode materials in electrochemical devices, particularly in supercapacitors. Therefore, there has been considerable scientific interest in vanadium pentoxide (V_2O_5) and its various oxidation states. Much work has been conducted to create different types of mixed metal oxide nanocomposite capacitive materials, and numerous research groups have employed metal vanadates (Mn, Ba, Zn, Cu, Ni, Co, Fe, etc.) as electrodes. Many guest species can intercalate at additional interlayer positions because of to the layered nature of V_2O_5 [30–32]. Furthermore, when amorphous VO*x* matrices were created electrochemically, there was a notable decrease in the aggregation of various metal species. Among many mixed trimetal vanadates, $BaZnV_2O_7$ has garnered significant attention because of its affordability, high specific capacity, environmental acceptability, and ease of availability.

The detection of analytes in solution is an essential precaution in the diagnosis of diseases in humans and animals [33]. The important chemicals ascorbic acid (AA) and uric acid (UA) are present in the human blood and are involved in various metabolic processes. Owing to their antioxidant properties, these acids can be employed in the prevention and treatment of a variety of illnesses, including mental illness, cancer, acquired immune deficiency syndrome (AIDS), and

common cold [34]. In addition to being a valuable antioxidant, AA is used in food, cosmetics, and animal feed. It also has many other applications in the body. The central nervous system contains AA at millimolar concentrations; therefore, it is critical to devise a quick, easy, and accurate method to detect this acid. Heavy metal ion contamination of the environment and water is an acute issue that poses a hazard to human life [35]. Heavy metal ions are dispersed throughout the air, water, and soil owing to an increase in industrial activity and the use of herbicides, insecticides, and paints in the contemporary society. Therefore, it is imperative that these heavy metal ions be detected quickly and accurately. Many instrumental techniques have been used to detect heavy metal ions, including electrolyte cathode atmospheric glow discharge, laser-induced breakdown spectroscopy, atomic absorption spectroscopy, inductively coupled plasma atomic emission spectroscopy, and microwave plasma torch-atomic emission spectroscopy. The aforementioned techniques are limited by the need for labor-intensive and complicated apparatus and pre-sample preparation [36]. Electrochemical biosensors, which have the benefits of speed, portability, easy sample preparation, and handling, have emerged as useful instruments to measure the components of aqueous matrices containing heavy metal ions and overcome the shortcomings of conventional approaches [37]. With the added benefits of sensitivity and specificity, electrochemical sensors have been explored as a means of detecting heavy metal ions. By appropriately altering the electrode surface using different nanomaterials (both organic and inorganic), electrochemical sensors can further increase their sensitivity and selectivity [38–40].

In this study, we explored the multifunctional properties of BZV NPs for enhanced photocatalysis, energy storage, and sensing applications. They were synthesized by the solution combustion method, which is scalable and cost-effective and characterized using various techniques for structural and morphological investigations. The photocatalytic properties were investigated under UV light for the effective degradation of AB-52 dye. The energy-storage performance of the BZV-modified carbon-paste electrode was evaluated using cyclic voltammetry (CV) and galvanostatic charge–discharge (GCD) techniques. The electrochemical sensing properties of the prepared nanoparticles and their limits of detection (LODs) to detect biomolecules, drugs, and heavy metals were measured using CV.

2. Materials and methods

Analytical reagent (AR)-grade materials used to synthesize BZV NPs were sourced from Sigma Aldrich. Unless specified otherwise, ammonium metavanadate (NH_4VO_3, ≥ 99.0% purity), urea (CH_4N_2O, 99.0% purity), barium nitrate ($Ba(NO_3)_2$, 99.0% purity), zinc nitrate ($Zn(NO_3)_2$), and AB-52 were employed in their as-received form.

2.1. Synthesis of BZV NPs

A mixture of 0.784 g of barium nitrate ($Ba(NO_3)_2$), 0.568 g of zinc nitrate ($Zn(NO_3)_2$), 0.702 g of ammonium metavanadate (NH_4VO_3), and 0.420 g of urea ($CO(NH_2)_2$) was combined in stoichiometric proportions, using urea as the fuel. The components were homogenized in 5 mL of water to ensure uniform dispersion. The resulting solution was transferred to a silica crucible and placed in a furnace preheated to (550 ± 10)°C. The mixture was maintained at this temperature for 5–10 min. As the solution dried, it ignited spontaneously, releasing significant amounts of gases such as CO_2, H_2O, and N_2, resulting in the formation of a foamy mass.

After combustion, the foamy product was removed, ground using an agate pestle and mortar, and then calcined at 900°C for 3 h [41]. A schematic representation of the combustion reaction is shown in Fig. 1, and the corresponding chemical equation can be expressed as follows:

$$3Ba(NO_3)_2 + 3Zn(NO_3)_2 + 6NH_4VO_3 + 7CO(NH_2)_2 \rightarrow 3BaZnV_2O_7 + 16N_2 + 26H_2O + 7CO_2 \quad (1)$$

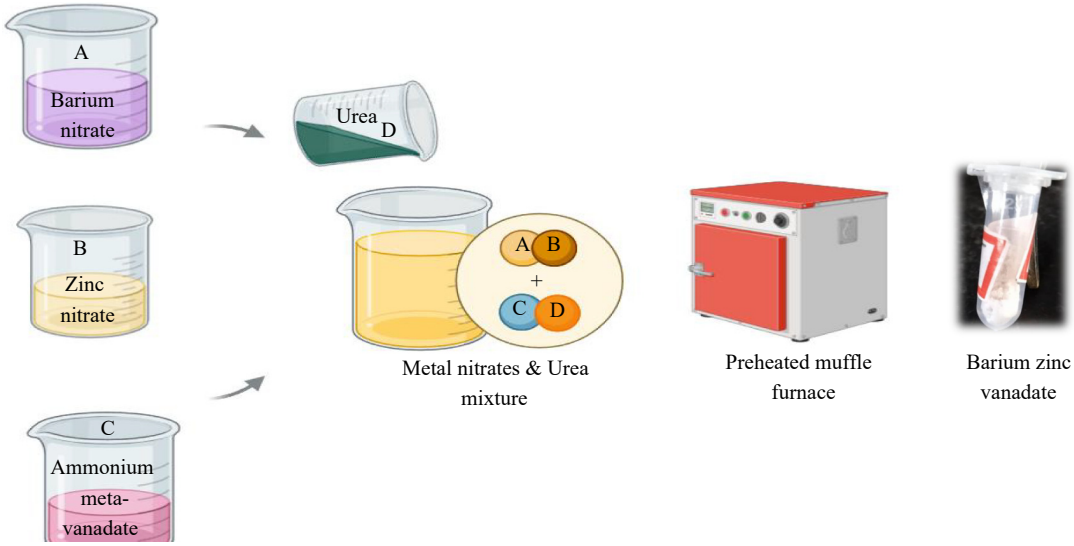

Fig. 1. Schematic representation of synthesis method.

2.2. Preparation of BZV modified carbon paste electrode (CPE)

To develop the modified carbon paste electrode (MCPE), graphite powder, a portion of the BZV sample combination, and a suitable quantity of mineral oil (silicon oil, 2–3 drops) were manually mixed in a mortar and pestle. A Teflon tube was filled to the maximum with this mixture. A copper pin was pressed into the Teflon and the rear of the mixture to create an electrical contact. A piece of butter paper was used to smooth out the BZV-modified CPE cavity.

3. Characterization

To determine the crystal structure and phase composition of the generated materials, X-ray diffraction (XRD) patterns were recorded using a Philips' X-pert Pro diffractometer that employed a Cu-K_α radiation source at 0.15406 nm, a 2θ range of 10°–80°, and a scan speed of $10°\cdot min^{-1}$. Infrared spectra of the as-prepared materials were obtained using a Shimadzu IRAffinity-1S MIRACLE 10 Fourier transform infrared (FTIR) spectrometer. KBr pellets at room temperature in the wavenumber range of 400–4000 cm^{-1} were used for the analysis. Diffuse reflection spectroscopy (DRS) measurements were performed on an ultraviolet-visible-near infrared (UV-vis-NIR) Shimadzu UV-vis (UV-2600) spectrophotometer using $BaSO_4$ powder as a standard reference. The morphology and elemental composition study was conducted under a microscope utilizing energy-dispersive X-ray spectroscopy (EDAX, VEGA3 TESCAN), a scanning electron microscope (SEM), a high-resolution transmission electron microscopy (HR-TEM) and X-ray photoelectron spectroscopy (XPS). A platinum wire, Ag/AgCl, and modified barium zinc vanadate-carbon paste electrode (MBZV-CPE) were employed as the counter and reference electrodes, respectively, in the electrochemical studies using a CHI608E potentiostat equipped with a tri-electrode system.

4. Results and discussion

4.1. XRD studies

BZV NPs were prepared using a standard combustion synthesis process, and XRD measurements were used to verify the crystal structure and phase purity of the resultant BZV NPs. As seen in Fig. 2(a), the data originated between $2\theta = 20°$ and 75°. This illustrates that the majority of the reflection peaks were indexed to BZV in accordance with JCPDS number 00-046-0759. The peaks identified in the $BaZnV_2O_7$ diffraction pattern can be associated to an orthorhombic phase with space group number 62 and space group *Pnma* ($a = 6.59$, $b = 8.38$, and $c = 9.47$; $\alpha = \gamma = 90°$ and $\beta = 100.17°$). The results show that organically generated BZV nanoparticles exhibited pure physical phases. The average crystallite size (D) was determined to be 40.3 nm using the Debye–Scherrer equation [41–42].

$$D = \frac{K\lambda}{\beta_\theta \cos\theta} \tag{2}$$

This equation includes the diffraction angle (θ), full-width half-maxima (FWHM, β_θ), X-ray wavelength ($\lambda = 1.54 \times 10^{-10}$ m), and diffraction constant ($K = 0.9$). These factors must be considered when examining XRD patterns to precisely determine the crystallite size.

It is evident from Eqs. (2) and (3) that strain changes (ε) as $\tan\theta$, whereas peak width from crystallite size varies as $\beta_\theta\cos\theta$. Williamson and Hall examined the peak width as a function of the diffracting angle 2θ and suggested a way to differentiate between size and strain broadening. They derived the following mathematical expressions:

$$\beta_\theta = \left(\frac{K\lambda}{D\cos\theta}\right) + (4\varepsilon\tan\theta) \tag{3}$$

which can be rearranged as:

$$\beta_\theta\cos\theta = \left(\frac{K\lambda}{D}\right) + (4\varepsilon\sin\theta) \tag{4}$$

A plot with $\beta_\theta\cos\theta$ along the y-axis and $4\sin\theta$ along the x-axis was made for the prepared BZV NPs (Fig. 2(b)). The preferred orientation peaks of BZV were plotted. Determining a crystallite size of 40.3 nm involved stretching the y-intercept of the fit to the data. Phase purity and crystallinity are crucial characteristics that significantly impact the performance of BZV NPs in both photocatalytic and electrochemical applications. A well-ordered atomic structure, indicated by a high degree of crystallinity, improves charge separation, re-

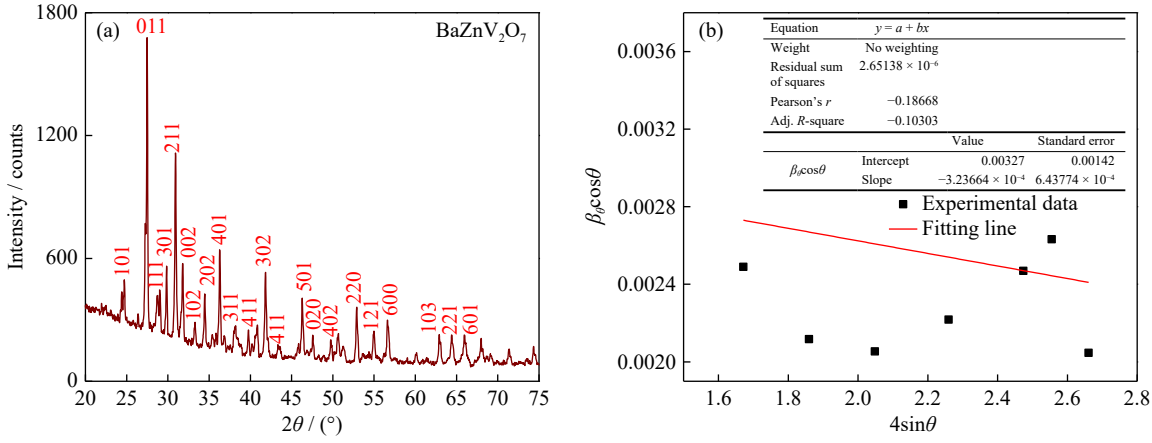

Fig. 2. (a) XRD patterns of BZV NPs and (b) Williamson–Hall (W–H) plot of BZV NPs.

duces electron-hole recombination, and increases photocatalytic performance. High crystallinity was indicated by sharp, powerful peaks in the XRD patterns, and phase purity was confirmed by the absence of extraneous peaks, indicating a single desired phase. The high phase purity of the BZV NPs indicates assurances that the substance is free of contaminants that can impair their functionality. When combined, these qualities improve the overall efficacy, stability, and efficiency of the materials for the purposes for which they are designed.

4.2. FTIR studies

FTIR spectroscopy was used to characterize the micro- and nano-structured substances to investigate their local structures. Fig. 3 shows the FTIR spectrum of BZV NPs. According to earlier findings, a sequence of absorption peaks induced by different vibration modes of V=O, and H–O–H emerges at 810 and 1113 cm^{-1}, respectively [43–45]. The Zn–O stretching mode has been identified as the cause of the band observed at 742 cm^{-1} and a less intense band at 681 cm^{-1}, which correspond to V–O–V and Zn–O–V asymmetric vibrations, respectively [46–47]. The stretched OH groups can be attributed to the broad band at 2309 and 2877 cm^{-1}. Traces of adsorbed water molecules are characterized by the band at 3539 and 3754 cm^{-1} [48]. The presence of ZnO in the nanoparticles is linked to the Zn–O stretching vibrations. As a result, ZnO is capable of creating reactive oxygen species (ROS) including hydroxyl radicals (·OH) and superoxide radicals ($\cdot O_2^-$) when exposed to UV light, it is well known for having strong photocatalytic activity. These ROS are highly effective in degrading organic contaminants. The existence of vanadate groups is indicated by the V–O stretching vibrations. Photogenerated charge transporters (electrons and holes) can be better separated by vanadate ions, which act as electron acceptors. Increased charge separation lowers the rate of electron-hole pair recombination, which boosts the photocatalytic efficiency [49].

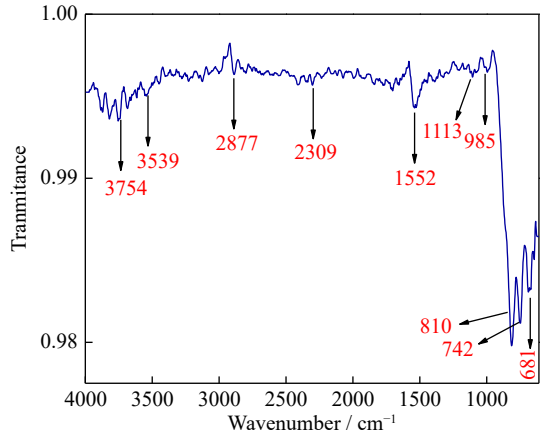

Fig. 3. FTIR spectrum of BZV NPs.

4.3. UV-Visible DRS (UV-DRS) studies

Fig. 4(a) shows the solid UV-DRS spectrum of the BZV NPs. The UV-vis diffuse reflectance spectra can be used to determine the band gap (E_g). With λ representing the wavelength, the bandgap energy (E_g) values were computed using the formula $E_g = 1240 / \lambda$ [50]. The broad bandgap makes it easier for the material to perform. The light absorption in the UV region is significantly enhanced by the BZV NPs.

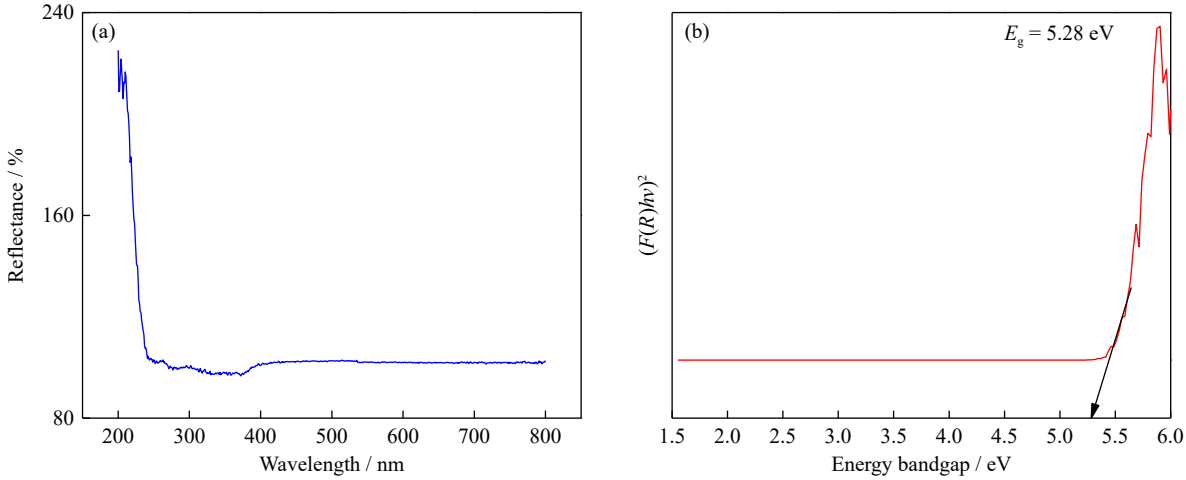

Fig. 4. (a) UV-DRS spectrum and (b) Kubelka–Munk bandgap plot of BZV NPs. *F*(*R*) represents the Kubelka–Munk fuction.

A higher absorption capacity in the UV light region is demonstrated by the BZV NPs. The BZV NPs absorption edge, which is approximately 250 nm, demonstrates its potent light-absorbing capacity in the UV light spectrum. Consequently, the high bandgap of BZV NPs makes them powerful photon absorbers. The direct bandgap was estimated using the Kubelka–Munk function. The direct bandgap value was estimated as 5.28 eV (as shown in Fig. 4 (b)). An orthorhombic crystalline phase is ensured by a bandgap energy of 5.28 eV for BZV [51], which clearly indicates that it is an effective UV-light-driven photocatalyst produced by combustion. With a relatively high bandgap of 5.28 eV, $BaZnV_2O_7$ mainly absorbs UV light rather than visible light. The consumption of the visible spectrum, which comprises a substantial amount of solar light, is restricted by this large bandgap. Therefore, under natural sunlight, the photocatalyt-

ic efficacy would be lower than that of materials with lower bandgaps, which are better at absorbing visible light.

4.4. SEM and EDAX studies

Scanning electron microscopy (SEM) analysis was performed to determine the morphologies of the $BaZnV_2O_7$ products. The characteristic morphology of the $BaZnV_2O_7$ compounds is shown at various magnifications in Fig. 5(a) and (b). The particles in this image are in the nanoscale, and the majority have a compact, self-assembling, egg-like shape. Furthermore, certain particles exhibit crystalline behavior, resulting in uneven forms and self-assembled configurations. The chemical purity and elemental composition of BZV NPs were assessed and confirmed by energy-dispersive X-ray spectroscopy (EDAX) mapping. The findings of the EDAX investigations shown in Fig. 5(c) verify that only four elements are present in the BZV NPs: Ba, Zn, O, and V. An EDAX examination revealed that some minor impurities were present without the detection limit. Their light absorption characteristics may also be affected by their distinctive shape. Structures that correspond to an egg-like structure may be efficient in scattering light, which would boost the photocatalytic activity and UV light usage. Compared to spherical, rod-shaped nanoparticles, the egg-like morphology usually offers a greater surface area, which can improve dye molecule adsorption onto the nanoparticle surface and increase the photocatalytic destruction efficiency.

4.5. HR-TEM studies

The morphology of the BZV NPs generated during combustion was examined using HR-TEM. The obtained images revealed that the morphology of the samples was composed of microstructures that resemble spheres and have a diameter of approximately 100–200 nm (Fig. 6(a) and (b)). An HR-TEM image of the BZV nanoparticles is shown in Fig. 6(c), where an interplanar distance of 0.38 nm is noted. Crystallite size measurements were performed using the Image-J software to acquire a more accurate particle size distribution. With a fluctuation of less than 10%, the average crystallite size of 43 nm is in good agreement with the values derived from XRD and the W–H method. Furthermore, a *d*-spacing of 0.412 nm was confirmed from the selected region electron diffraction (SAED) pattern shown in Fig. 6(d), further validating the BZV NP crystalline structure.

4.6. XPS studies

The XPS profiles of the prepared sample, shown in Fig. 7, provide critical insight into the elemental compositions and oxidation states of the constituent elements. The survey spectrum in Fig. 7(a) identifies three cations, Ba, Zn, and V, along with an anion, O. For Ba, the binding energy peaks at 779.3 and 794.5 eV, depicted in Fig. 7(b) exhibit single components, confirming the uniform oxidation state of 2+. Similarly, Fig. 7(c) presents the XPS spectrum for Zn, where peaks at 1021.4 and 1044.6 eV correspond to the $2p_{3/2}$ and $2p_{1/2}$ states

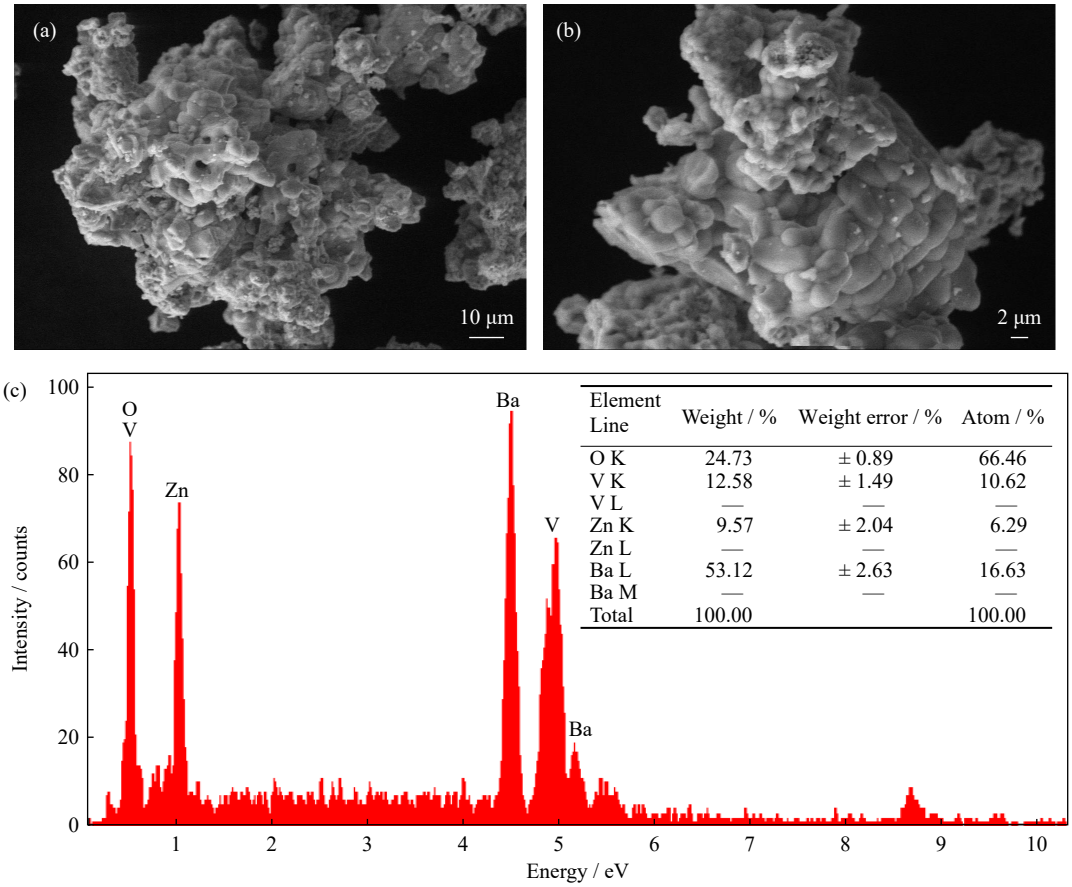

Element Line	Weight / %	Weight error / %	Atom / %
O K	24.73	± 0.89	66.46
V K	12.58	± 1.49	10.62
V L	—	—	—
Zn K	9.57	± 2.04	6.29
Zn L	—	—	—
Ba L	53.12	± 2.63	16.63
Ba M	—	—	—
Total	100.00		100.00

Fig. 5. SEM images of BZV NPs at the magnification of (a) 5000×, (b) 2000×. (c) EDAX spectrum.

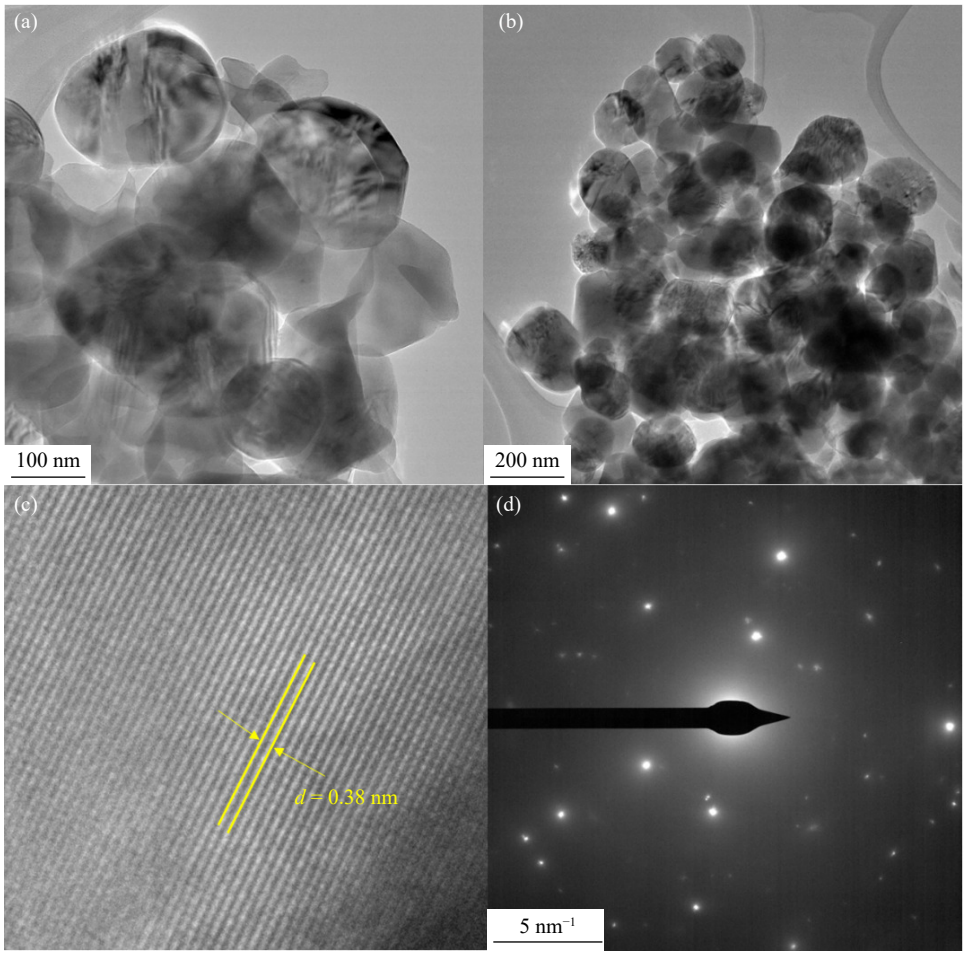

Fig. 6. TEM micrographs at (a) 100 nm and (b) 200 nm. (c) HR-TEM images of BZV. (d) SAED pattern of BZV NPs.

of Zn, respectively, also indicating a single oxidation state of 2+. For V, Fig. 7(d) shows peaks at 517 eV for the $2p_{3/2}$ state and another peak at 524 eV for the $2p_{1/2}$ state, consistent with the oxidation state of 5+. The oxygen peak, deconvoluted into two components at 529.5 and 531.3 eV, suggests the presence of two distinct chemical environments, attributable to interactions with V^{5+}, Zn^{2+}, or Ba^{2+}, as shown in Fig. 7(e).

The XPS analysis confirms the oxidation states of the elements in the compound as Ba^{2+}, Zn^{2+}, V^{5+}, and O^{2-}, validating the chemical composition of $BaZnV_2O_7$. These findings align well with previously published results [52], further corroborating the conclusions of this study.

5. Photocatalytic degradation studies of AB-52 dye under UV light

The AB-52 dye was subjected to collective UV photocatalytic degradation for a consistent 120-min test period. Within the photoreactor, the beaker placed on a magnetic stirrer had a working capacity of 250 mL. To study several parameters, such as the photocatalyst dose (20–100 mg), dye concentration (5–25 ppm, mass fraction), pH (2–10), and UV light irradiation (125 W mercury bulb), the range of each parameter was varied, while the others remained fixed. Samples of the reaction mixture were removed at the completion of the experiment and examined for color and degradation percentage. These results were compared with the initial measurements of these parameters to evaluate the efficacy of the UV photocatalytic removal. Studies were conducted on the UV photocatalytic degradation of the AB-52 dye under fully optimized conditions. A UV-vis spectrophotometer was used to measure decolorization, which was defined as a decrease in absorbance at 508 nm. Eq. (5) was used to determine the degradation percentage [53]:

$$\text{Degradation percentage} = \frac{A_0 - A}{A_0} \times 100\% \quad (5)$$

where A_0 and A are the absorbance values of the sample at 0 min and t min, respectively. The experiment was repeated thrice to perform error analysis, and error bars (2% to 3%) have been shown in all degradation graphs.

5.1. Impact of photocatalyst dosage

AB-52 degradation was observed when exposed to varying doses of the BZV photocatalyst (20–100 mg) in 250 mL of dye solution. Each photoreaction was performed for 120 min. As the catalyst dose is raised, a significant number of catalytically active sites are created, boosting the rate of $\cdot O_2^-$ and ·OH production. Excess catalyst prevents light penetration and causes a decrease in the rate of degradation, starting at 40 mg [54]. The outcomes are shown in Fig. 8(a). Thus, 40 mg/250 mL was determined as the ideal catalyst dose for the reactor. The effective surface area of the photocatalytic

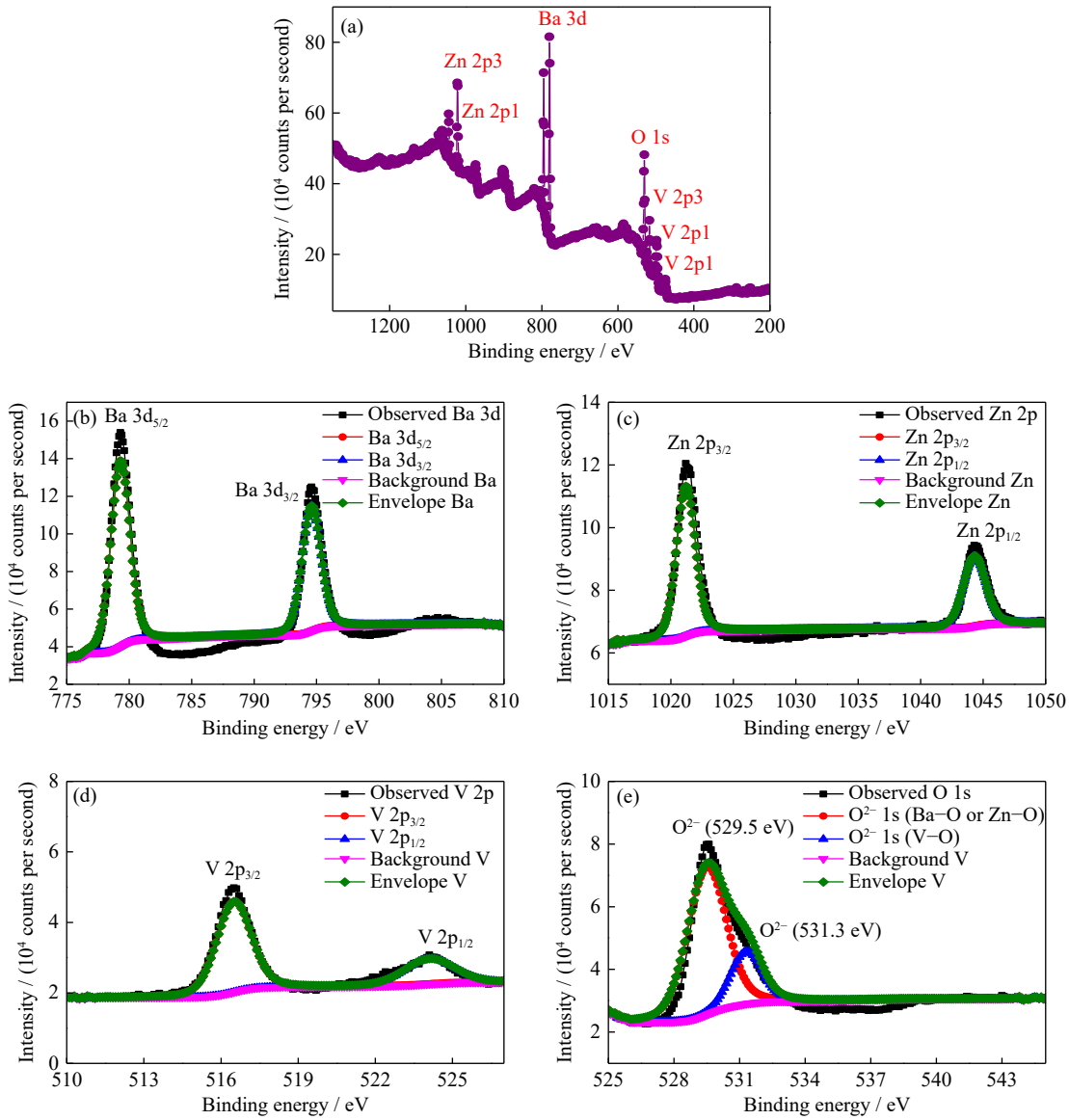

Fig. 7. (a) Total XPS spectrum of the BZV NPs, XPS of (b) Ba, (c) Zn, (d) V, and (e) O.

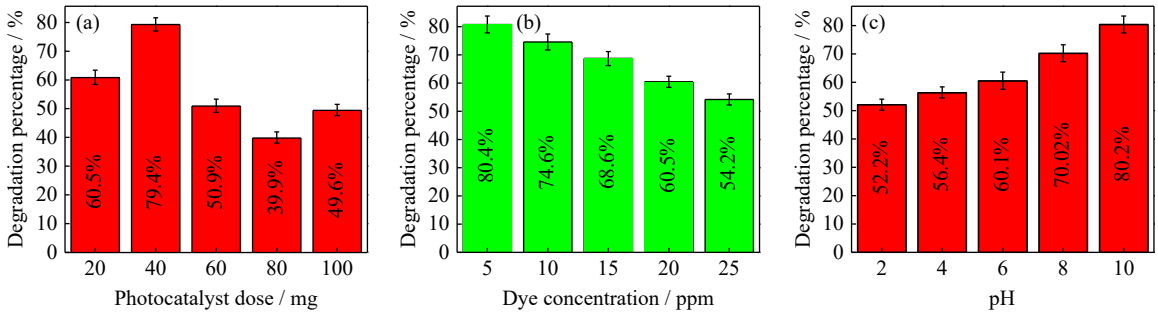

Fig. 8. Photocatalytic AB-52 degradation factors include (a) photocatalytic dosage, (b) dye concentration, and (c) pH.

reaction decreases when the particles aggregate. This restricts the number of active sites that dye molecules can adsorb and decrease. The separation of charges and interaction processes of photogenerated electron-hole pairs, which are essential for the photocatalytic process, can be affected by agglomeration. Photocatalytic efficiency may decline because of inadequate charge separation.

5.2. Effect of initial concentration of AB-52 dye on photocatalytic degradation

The effect of the AB-52 dye concentration on the degradation efficiency was evaluated. After the photoreaction for 120 min with 10 mg of the BZV photocatalyst, the degradation percentages were determined. The results of the evaluation of various initial AB-52 dye concentrations (5–25 ppm,

mass fraction) are shown in Fig. 8(b). As the dye concentration increased, more dye fragments got absorbed over the surface of the catalyst [55]. The extra fragments prevent light from penetrating, reducing the production of active sites during the photoreaction. The photocatalytic efficiency dramatically decreased because of fewer active sites. Thus, less light harvesting results in fewer active sites on the catalyst, and more photogenerated charges are expected for dye degradation as a result of increased photon absorption at the catalyst surfaces. Furthermore, because the catalyst quantity stays constant, the photo-catalytically generated ·OH and $\cdot O_2^-$ on the photocatalyst surface also stays constant. To maintain equilibrium while the amount of catalyst is fixed, it is common for increasing dye concentrations to require higher concentrations of ·OH and $\cdot O_2^-$ reactive species [56].

5.3. Influence of pH

The primary determinant of dye degradation is solution pH [57]. It is evident that changing the pH concentration affects the chemical properties of the catalysts and dye that must be broken down. To examine the pH factor, the reaction mixture/analyte solution was mixed with the reagents HCl and NaOH (Alfa chemicals, analytical grade) to preserve its pH. For each photoreaction, 40 mg of BZV catalyst and 5 $mg \cdot L^{-1}$ of AB-52 dye were added, and the pH range was established between 2 and 10. Similarly, the effect of pH was assessed by optimizing the temperature at room temperature for 120 min. Because of its strong affinit for the catalyst surface, AB-52 shows a slow degradation rate under acidic pH conditions [58]. In addition, BZV develops a higher oxidation state and loses its metallic properties at acidic pH values. However, the presence of a large number of hydroxide ions and their higher capacity to be transformed into ·OH caused the degradation rate of AB-52 to accelerate at alkaline pH. Therefore, the BZV photocatalysts could operate effectively in alkaline media because of the increased adsorption of cationic dyes on their surfaces. Fig. 8(c) shows the photodegradation rate of AB-52 on BZV as a function of pH. The protonation state of the dye molecules can be influenced by the pH of the solution. Owing to their increased protonation at low pH (acidic conditions), the dye molecules may be less reactive with the photocatalyst. In contrast, dye molecules are more deprotonated at high pH (alkaline conditions), which increases their reactivity and accelerates their decomposition. The production of reactive species, including superoxide radicals ($\cdot O_2^-$) and hydroxyl radicals (·OH), can be influenced by pH. When hydroxide ions (OH^-) are present in an alkaline environment, more hydroxyl radicals can develop. These radicals are highly efficient at breaking down organic pollutants [59].

5.4. Effect of sacrificial agents (scavengers)

The differences in AB-52 dye degradation before and after sacrificial agents were noted to determine the function of the active species, which include holes (h^+), electrons (e^-), and hydroxyl groups (·OH). The BZV photocatalyst produces ·OH when exposed to UV light through the interaction of the adsorbed H_2O with h^+. By interacting with e^-, adsorbed O_2 also yields $\cdot O_2^-$. According to the sacrificial agent, one of the primary reactive species produced by BZV systems is $\cdot O_2^-$. Silver nitrate ($AgNO_3$), ethanol, and ethylene diamine tetraacetate (EDTA) were used as sacrificial agents to capture electrons (e^-), hydroxyl radicals (·OH), and holes (h^+), respectively.

After adding 1 mM of e^- scavenger $AgNO_3$, the degradation efficiency of BZV decreased to 37.35%. However, the degradation percentage decreased to 35.25% when 1 mM of EDTA (h^+ scavenger) was added, indicating that holes contributed to dye degradation. The degradation efficiency reduced to 27.90% by 1 mM ethanol (·OH scavenger), suggesting that ·OH plays a major role in the photocatalytic activity [60]. Hydroxyl radicals are particularly significant during the photocatalytic process. Because the photogenerated electrons of the photocatalyst have a higher reduction potential than $\cdot O_2^-/O_2$, the released electrons could be readily transferred to the oxygen (O_2) molecules adsorbed on the BZV photocatalyst surface, creating superoxide ($\cdot O_2^-$), a potent oxidizing species that breaks down organic molecules. When scavengers were applied, only 37.35% of the AB-52 dye was broken down, whereas 80.4% of the dye was broken down in the absence of sacrificial agents. Therefore, it is evident from the data in Fig. 9 that scavengers significantly inhibit the degradation of the AB-52 dye.

5.5. Enhanced photocatalytic degradation mechanism of AB-52 dye

Fig. 10 illustrates the mechanism of photocatalytic activity (PCA) and the production of holes and electrons in the BZV NPs under UV light illumination for the sequential decomposition of the AB-52 dye. Excitation occurs when photons with energies equal to or greater than the semiconductor's optical bandgap energy interact, creating and separating electron-hole pairs in a stimulatory manner. The conduction band (CB) photo stimulated electrons transform the surface-adsorbed oxygen (O_2) molecules into superoxide anion radicals ($\cdot O_2^-$). A hydroxyl radical (·OH) species is produced when hydroxyl (OH^-) ions are oxidized by photogenerated holes in the valence band (VB). Superoxide $\cdot O_2^-$ and hydroxyl ·OH radicals, particularly ·OH, which is an effective oxidizing agent, convert dye molecules into less dangerous by-products and cause water to mineralize, producing CO_2 and H_2O [61].

The following equations can be used to explain photo-induced reactions and electron-hole transfer on the BZV photocatalyst surface.

$$BZV + UVlight \rightarrow BZV(e^- + h^+) \quad (6)$$

$$h^+ + H_2O \rightarrow \cdot OH + h^+ \quad (7)$$

$$O_2 + e^- \rightarrow \cdot O_2^- \quad (8)$$

$$\cdot O_2^- + h^+ \rightarrow \cdot OH \quad (9)$$

$$BZV(e^-) + \cdot O_2^- + 2h^+ \rightarrow BZV + H_2O_2 \quad (10)$$

$$BZV(e^-) + H_2O_2 + e^- \rightarrow BZV + \cdot OH + OH^- \quad (11)$$

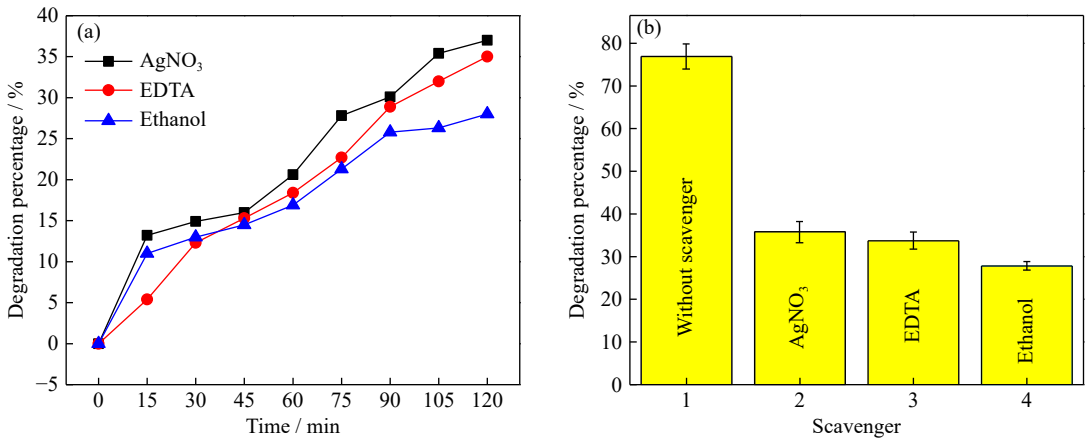

Fig. 9. Degradation percentage variation for different (a) scavengers with respect to time and (b) scavengers.

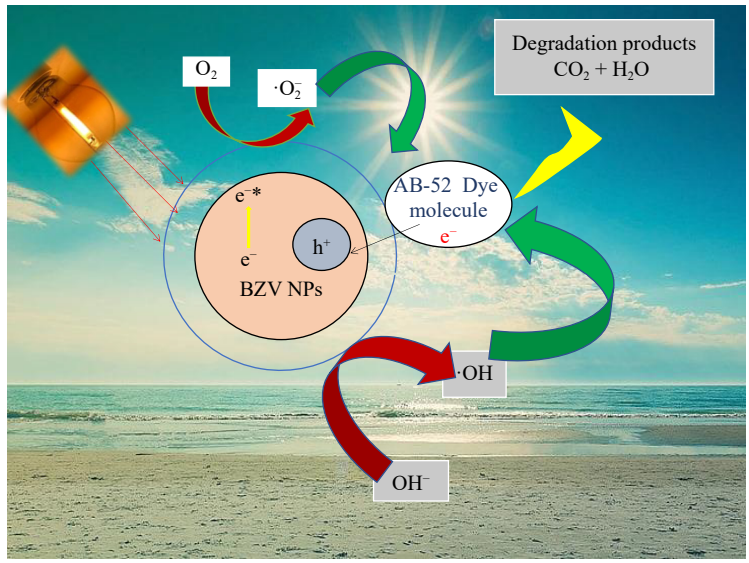

Fig. 10. Photocatalytic degradation of AB-52 dye.

$$\text{AB-52 dye} + O_2 + {\cdot}O_2^- + {\cdot}OH \rightarrow \text{degraded products } (CO_2 + H_2O) \quad (12)$$

Table 1 highlights the superior photocatalytic performance of BZV NPs synthesized using the combustion method, achieving 80.4% degradation of AB-52 dye under UV light [62–78]. This efficiency surpasses other materials such as MgO (70%), NiO (79%), and $BiVO_4$ synthesized via co-precipitation (72.72%). The table underscores the edge of $BaZnV_2O_7$ over its counterparts, which is attributed to its optimized synthesis method and favorable structural and optical properties. These results validate its potential as a cost-effective and environmentally friendly photocatalyst for efficient dye degradation in wastewater treatment.

6. Electrochemical studies

6.1. CV studies

CV, electrochemical impedance spectroscopy (EIS), and galvanostatic charging and discharging (GCD) studies were used to assess the electrochemical characteristics of BZV NPs. CV provides insight into the capacitive properties of materials. Fig. 11(a) shows the CV curves of the BZV NPs in a 1 M KCl electrolyte with a scan rate ranging from 5 to 100 $mV \cdot s^{-1}$. The quasi-rectangular form of the BZV electrode in the KCl electrolyte is clearly visible. Electrode materials for batteries and EDLCs store charge via different processes. The battery processes are faradaic, whereas the EDLC processes are electrostatic. These different electrode behaviors can be clearly distinguished by the shape and scan rate (v) dependence of the cyclic voltammograms.

Indeed, battery electrodes feature peak-shaped CV current–potential responses proportional to v, whereas EDLC electrodes exhibit a quasi-rectangular response with currents proportional to v. Pseudocapacitive materials represent a different class of electrodes. Pseudocapacitance originates from a fast faradaic process that takes place at the surface or near-surface of the electrode material and that, in parallel, gives rise to a capacitive signature, that is, a quasi-rectangular CV response with currents proportional to v [79]. This demonstrates the superior capacitance of the electrode materials. The ability of the BZV electrode material to store charge is aided by the intercalation of electrolyte ions, K^+. At a scan rate of 5 $mV \cdot s^{-1}$, the highest specific capacitance for KCl electrolyte was 714.15 $F \cdot g^{-1}$. The direct relationship between the scan rate and voltammetric current is well known. Similarly, when the potential sweep rate is changed, a sharp

Table 1. Comparison of photocatalytic efficiency with other nanoparticles

Compound	Synthesis method	Light source	Degradation percentage / %	Reference
NiO	Co-precipitation	UV	80	[62]
NiO	Combustion	UV	99.6	[63]
NiO	Sol–gel	UV	79	[64]
MgO	Combustion	UV	70	[65]
$BiVO_4$	Co-precipitation	UV	72.72	[66]
$BiVO_4$	Hydrothermal	Visible	98.21	[67]
(V_2O_5\ZnO\Pd)	Photoreduction method	UV	96	[68]
$BiVO_4$	Hydrothermal	Visible	68	[69]
V_2O_5	Co-precipitation	Visible	85	[70]
V_2O_5/RGO	Hydrothermal	UV	98.85	[71]
ZnO/CuO	Co-precipitation	UV	70.22	[72]
V_2O_5/PMMA films	Hydrothermal	UV	80	[73]
$Cd_2V_2O_7$	Sol–gel	UV	77	[74]
$SmVO_4$	Precipitation	Visible	70.99	[75]
$Co_3O_4/CuBi_2O_4/SmVO_4$	Ultrasonication	Visible	76.1	[76]
$Cr_2V_4O_{13}$	Green synthesis	UV	71.35	[77]
$LaVO_4/TiO_2$	Sol–gel	Visbile	57	[78]
$BaZnV_2O_7$	Combustion	UV	80.4	Present study

Noted: RGO represents reduced graphene oxide and CNTs respresents carbon nanotubes.

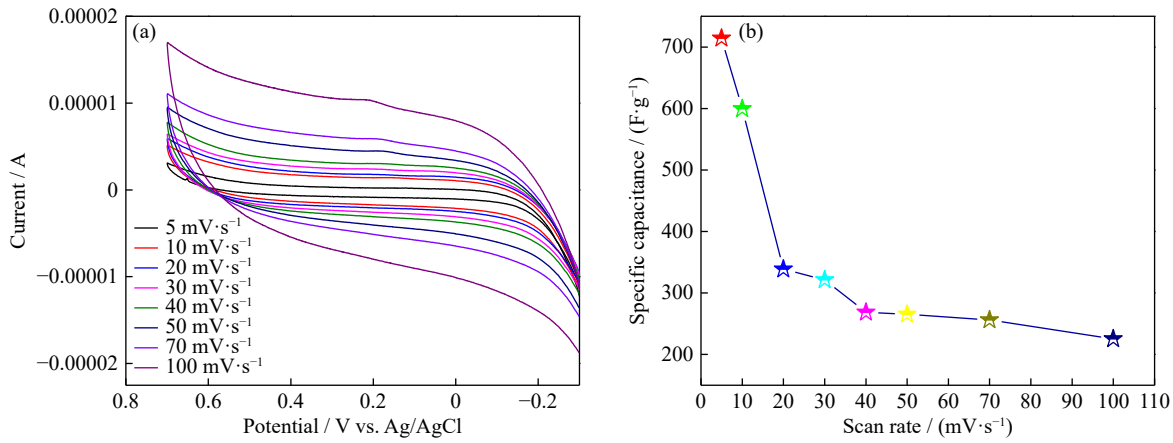

Fig. 11. (a) CV curves of BZV electrode and (b) specific capacitance of BZV electrode at different scan rate.

change in the current is evident. This indicates that the BZV electrode experiences faster and more reversible faradaic responses. Therefore, the form of the CV curve in the potential range of 0.7 to −0.3 V in an aqueous solution reveals the capacitive behavior of the material. Fig. 11(b) shows how the specific capacitance varies with a variable scan rate between 5 and 100 $mV \cdot s^{-1}$. The specific capacitance of BZV has been demonstrated to be larger at low scan rates, as the figure illustrates.

Electrolyte ions have sufficient time to flow through the active part of the electrode material for charge storage after fully diffusing into it, which is precisely what occurs. As the scan rate increases, the specific capacitance of the material decreases. The time constants at higher scan rates cause the electrolyte ions to intercalate into the innermost sites of the BZV component in the electrode to decrease [80]. This causes the CV curve to expand, with only the outer active surface contributing to charge storage. Consequently, the physical characteristics of ions, such as their conductivity, ionic radius, mobility, and ionic hydration sphere radius, determine the fluctuations in the current responsiveness and CV performance of BZV [81]. The K^+ and Cl^- ions have distinct ionic radii of 1.33 and 0.95 Å, although their hydration numbers are nearly the same. In addition to the ionic radius of the electrolyte, the specific capacitance of a material is also influenced by its ion mobility and conductivity. As a result, K^+ ions with a greater molar conductivity (7.35×10^{-3} $m^2 \cdot (\Omega \cdot mol)^{-1}$) can undoubtedly wander into the electrode/electrolyte surface to promote increased specific capacitance. Although the mobility of the K^+ cation will be hindered by the presence of Cl^- anions, the primary cause of the variance in capacitance values for BZV is the increased conductivity of the ion.

The specific capacitance (C_{sp}, $F \cdot g^{-1}$) of the BZV electrode is obtained by using Eq. (13).

$$C_{sp} = \frac{I}{v \times m} \tag{13}$$

Eq. (13) provides a function of current (I), scan rate (v),

and the weight of the material placed on the electrode (*m*).

Table 2 compares the specific capacitance of the BZV nanoparticles with those of other vanadate-based materials, highlighting their superior energy storage capabilities [82–92]. BZV synthesized using the combustion method has a specific capacitance of 714.15 $F \cdot g^{-1}$, significantly outperforming materials such as $SbVO_4$ (384 $F \cdot g^{-1}$) and $Zn_3(VO_4)_2$ (312 $F \cdot g^{-1}$) while being competitive with $Co_2V_2O_7$ (628 $F \cdot g^{-1}$) and $CuMg_2V_2O_8$ (560.5 $F \cdot g^{-1}$). The enhanced capacitance of BZV can be attributed to its unique morphological and structural properties, which allow efficient ion intercalation and charge storage. These findings suggest that BZV is a promising material for next-generation energy storage applications, combining its high performance with scalable and cost-effective synthesis.

6.2. EIS

EIS analysis was performed to observe the resistive and capacitive properties of the BZV electrodes. From EIS investigations conducted in the frequency range of 0.01 Hz to 1×10^5 Hz in KCl medium with MCPE, the real (Z') and imaginary (Z'') parts of the curve were obtained. The Nyquist curves for the BZV-modified electrode before and after GCD are shown in Fig. 12(a) and (b), respectively. As seen in Fig. 12(a), the impedance graph was fitted using an equivalent circuit. Both the charge transfer resistance and solution resistance are important parameters that affect the performance of a supercapacitor.

The electrochemical impedance spectrum was composed of three distinct regions: (i) the solution resistance (R_s), (ii) a semicircle in the high-frequency region corresponding to the charge-transfer resistance (R_{ct}), and (iii) a linear component in the low-frequency region indicating the Warburg resistance. The stable electrochemical efficiency of the asymmetric supercapacitor is indicated by the R_s values, which were 150 Ω before and after the GCD run, and the R_{ct} values, which were 1729 and 1842 Ω before and after the GCD run, respectively. It is clear that the faradaic redox reaction on the electroactive surfaces caused the resistance to increase [93]. In Fig. 12 (b) comparative graph has been shown which contain both before and after GCD curves to understand the difference in the frequency.

6.3. GCD

The GCD curves of the BZV electrode were collected at a current density in the range of 1–7 $A \cdot g^{-1}$, as illustrated in Fig. 13(a). Within the potential window of 0.24 to 0.369 V for the BZV electrode in relation to Ag/AgCl, as shown in the Fig. 13 (b), at 1 $A \cdot g^{-1}$, the measurements were carried out over 1000 cycles. These tests aimed to assess the long-term

Table 2. Comparison of results of other vanadates with the present work

Compound name	Synthesis method	Test condition	Specific capacitance / ($F \cdot g^{-1}$)	Reference
$SbVO_4$	Hydrothermal	Scan rate 5 $mV \cdot s^{-1}$	384	[82]
$Mn_2V_2O_7$	Chemical method	Scan rate 10 $mV \cdot s^{-1}$	528	[83]
MnV_2O_6	Hydrothermal	Current density 1$A \cdot g^{-1}$	1067	[84]
$Zn_3(VO_4)_2$	Co-precipitation	Current density 1$A \cdot g^{-1}$	312	[85]
$Zn_3(VO_4)_2$	Simple reflux	Scan rate 5 $mV \cdot s^{-1}$	104	[86]
$Ca_5Mg_4V_6O_{24}$	Solution combustion	Scan rate 10 $mV \cdot s^{-1}$	346.66	[87]
$Ba_{0.18}V_2O_{4.95}/NH_4V_4O_{10}$	Liquid-phase deposition method	Current density 210 $mA \cdot m^{-2}$	130.99	[88]
$CuMg_2V_2O_8$	Solution combustion	Current density 1 $A \cdot g^{-1}$	560.5	[89]
$CuMg_2V_2O_7$	Combustion	Scan rate 5 $mV \cdot s^{-1}$	242	[90]
$Na_2V_6O_{16}$	Ultrasonic-assisted chemical route	Current density 0.5 $A \cdot g^{-1}$	455	[91]
$Co_2V_2O_7$	Hydrothermal	Scan rate 5 $mV \cdot s^{-1}$	628	[92]
$BaZnV_2O_7$	Solution combustion	Scan rate 5 $mV \cdot s^{-1}$	714.15	Present work

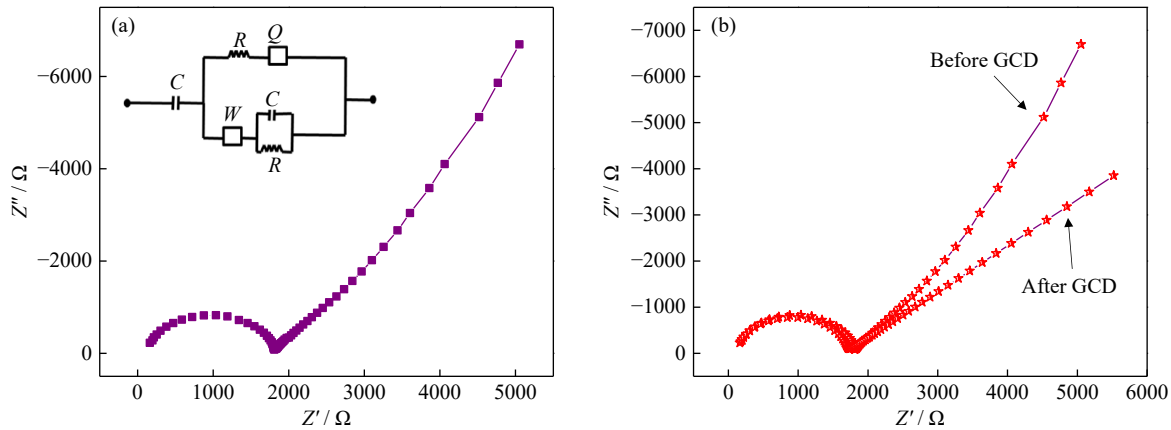

Fig. 12. EIS spectra of BZV electrodes (a) before GCD and (b) comparison of before and after GCD. *R*—resistor, *C*—capacitor, *W*—Warbug impedance, and *Q*—constant phase element.

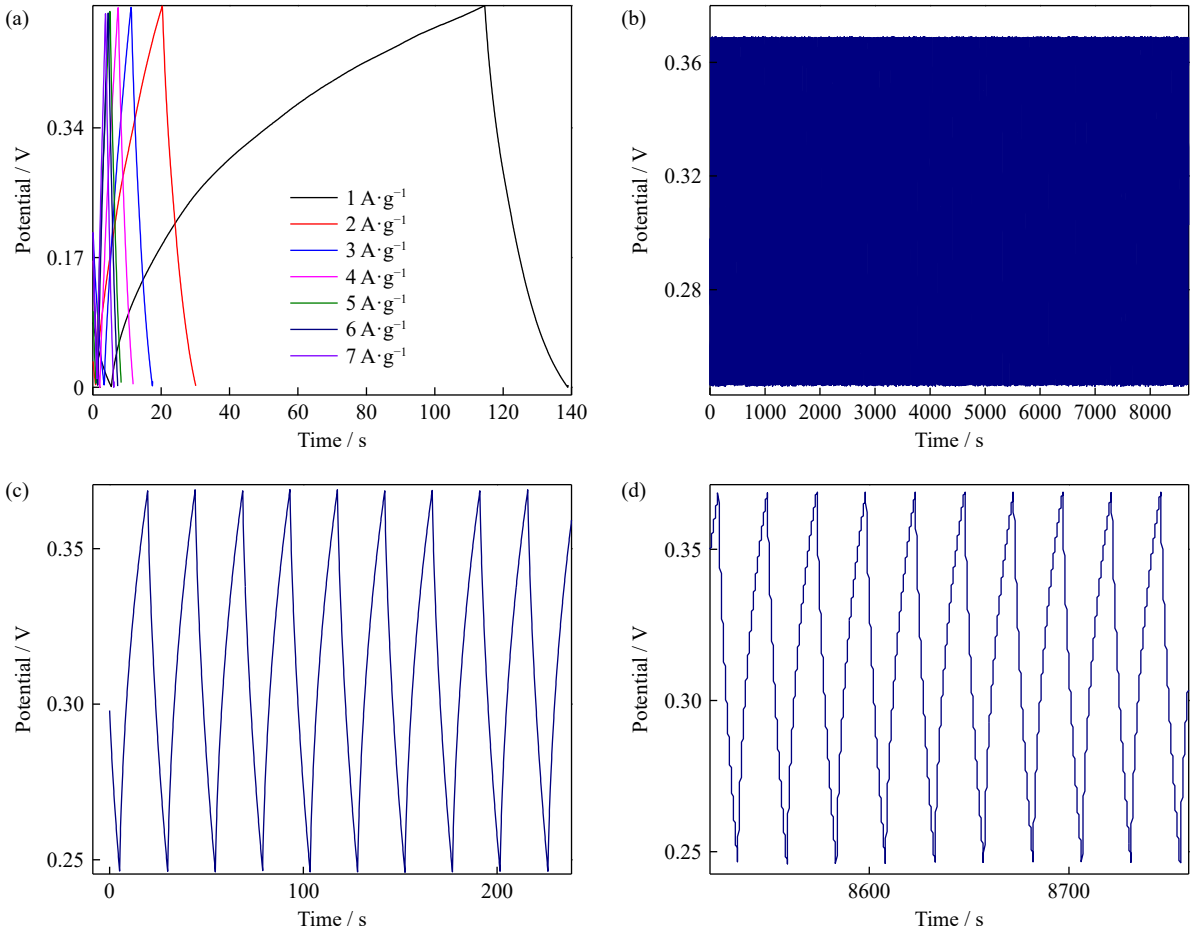

Fig. 13. GCD curves at (a) 1 to 7 A·g^{-1}, (b) 1000 complete cycles, (c) first 10 cycles, and (d) last 10 cycles.

stability of the electrodes. To determine the best electrolyte for the electrode material, the effect of the KCl electrolyte on the capacitance function of the supercapacitor was also examined. Plotting the charge and discharge components reveals a linear relationship, which is a feature of the rapid charge storage/release mechanism [94]. The symmetric charge–discharge curves show improved reversibility of the electrochemical performance of the BZVs. The expression given in Eq. (14) [95] was used to determine the electrode capacitance (C_p). The BZV electrode maintained over 90% of its initial capacitance even after 1000 cycles in 1 M KCl as shown in Fig. 13(c) and (d). This raises the possibility that the electrode was replaced during its initial activity, which would improve performance and increase capacity retention:

$$C_p = \frac{I \times dt}{m \times (V_f - V_i)} \tag{14}$$

where I is the applied current, dt is the discharging time, m is the mass of active material coated onto the electrode, and $(V_f - V_i)$ is the working potential window.

Table 3 presents the specific capacitances of the BZV electrodes derived from the CV and GCD measurements at varying scan rates. The results reveal a high specific capacitance of 714.15 F·g^{-1} at a low scan rate of 5 mV·s^{-1} (CV), which decreases with increasing scan rate, reaching 225.44 F·g^{-1} at 100 mV·s^{-1}. Similarly, GCD measurements indicate a specific capacitance of 857.4 F·g^{-1} for the first cycle at 5 mV·s^{-1}, slightly decreasing to 809.52 F·g^{-1} for the last cycle, demonstrating excellent retention over repeated cycles.

Table 3. Specific capacitance value from CV

Scan rate / (mV·s^{-1})	Specific capacitance / (F·g^{-1})
5	714.15
10	599.52
20	338.62
30	321.31
40	268.65
50	265.43
70	256.21
100	225.44

The decline in capacitance at higher scan rates is attributed to insufficient time for the electrolyte ions to diffuse into the inner active sites of the electrode material, limiting charge storage to the outer surface. The near-linear relationship observed in the charge–discharge profiles confirms a reversible and efficient energy storage mechanism. These findings underscore the potential of BZVs for high-performance energy storage owing to their high specific capacitances, excellent cyclic stabilities, and scalabilities.

7. Sensing application

7.1. Biomolecule sensing

CV measurements were made once the electrodes were

positioned and the potential range was adjusted from +0.8 V to −0.4 V. Following completion of the experiment, additional measurements were taken using the new BZV electrodes for additional analysis. Target biomolecule detection using the CV method with the sensor constructed with the BZV sensor is shown in Fig. 14. CV measurements were performed for each biomolecule in individual cells. The concentration of each biomolecule was raised within a predetermined range, and the capacity of the constructed sensors was tracked. UA concentration analysis was conducted in 1 M KCl, as shown in Fig. 14(a). It was noticed that the optimum potential was 0.1 V. For AA, the same steps were taken again (Fig. 14(c)). The peak potentials were recorded as −0.1 V. As shown in Table 4, the analytical figures of merit, including the linear range and detection limit, were independently determined in the presence of the corresponding values of AA and UA for the target molecules [96–97].

The limit of detection (LOD) represents the lowest analyte concentration that can be reliably distinguished from the background noise. This can be calculated using the following equation:

$$\mathrm{LOD} = \frac{3M}{S} \tag{15}$$

where M is the standard deviation, and S is the slope of the calibration curve (sensitivity of the method).

7.2. Chemical drug sensing

Paracetamol and ibuprofen were electrochemically detected using BZV NPs synthesized in this study. The electro-

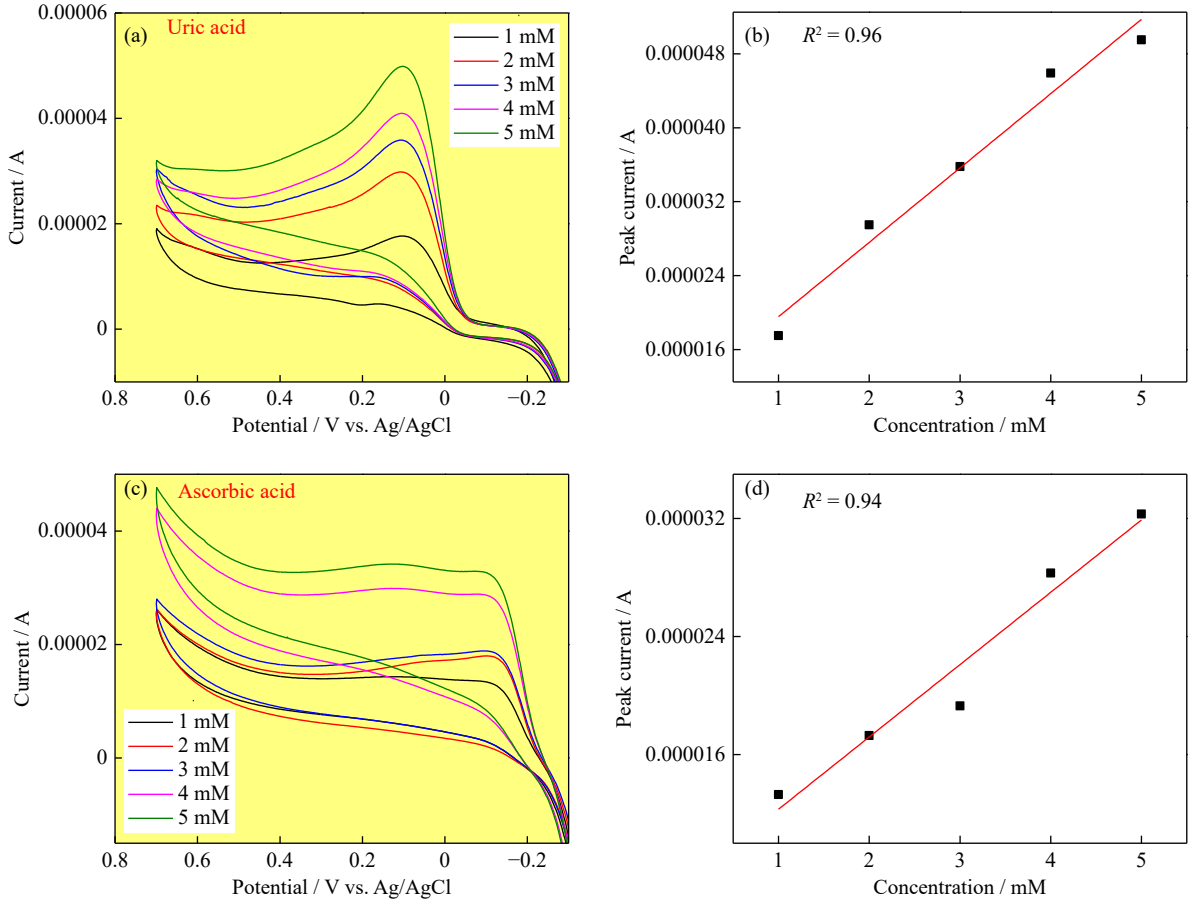

Fig. 14. Electrochemical sensing performance for uric acid and ascorbic acid: CV curves of the sensor in the presence of (a) UA and (c) AA at varying concentrations; calibration plots of the oxidation peak current versus concentration derived from the CVs for (b) UA and (d) AA.

Table 4. Detection limit of different types of molecules.

Content	R^2	Limit of detection (LOD) / (mol·L^{-1})
Uric acid	0.96	0.11×10^{-6}
Ascorbic acid	0.94	0.57×10^{-6}
Paracetamol	0.99	0.58×10^{-6}
Ibuprofen	0.95	0.11×10^{-6}
Mercury	0.87	0.39×10^{-6}
Cobalt	0.89	0.57×10^{-6}
Cadmium	0.95	0.31×10^{-6}

chemical redox behavior of ibuprofen and paracetamol was investigated in BZV using CV. The chemical drug-sensing CV curves are shown in Fig. 15. In the figure, there are no discernible redox peaks for the BZV. Paracetamol anodic peaks at −0.027 and 0.37 V, similarly ibuprofen anodic peak at 0.23 V can be observed in the voltammograms of paracetamol and ibuprofen acquired for the BZV electrode. Oxidation may have caused the measured redox peak. Compared to a sensor-free system, BZV exhibits distinct redox peaks and better current responsiveness. This demonstrated the strength of the electrocatalytic activity of the electrode [98]. This implies that the BZV layer has rapid electron transport and strong electrochemical activity and that the electrode reaction is consistent with the mechanism that is regulated by diffusion [99]. According to the electrochemical data, a catalytic process involving BZV, paracetamol, and ibuprofen allowed molecules to transfer electrons to the modified electrode. This facilitated the electrochemical oxidation of these medications. This is because the produced BZV NPs can accelerate electron transfer by acting as catalysts. Therefore, it is evident that BZV can be effectively applied for the electrochemical detection of chemical drugs such as ibuprofen and paracetamol.

7.3. Heavy-metal sensing

To determine the sensitivity, CV was used as an analytical method to efficiently detect Hg^{2+}, Co^{2+}, and Cd^{2+}. An modified carbon paste electrode was used to detect these chemicals using CV. Heavy metal concentrations between 1 and 5 mM were studied for BZV NP sensing. The Hg^{2+}, Co^{2+}, and Cd^{2+} redox peaks are depicted in Fig. 16(a)–(f), respectively. The modified BZV electrode exhibits three distinct peaks for Hg^{2+}, Co^{2+}, and Cd^{2+} at 0.08, 0.15, and 0.194 V versus Ag/AgCl, respectively. Based on the results of cyclic voltammetry, the catalytic activity of BZV was also applied to the redox reactions of Hg^{2+}, Co^{2+}, and Cd^{2+}. In the oxidation–reduction current peak, the level of sensitivity or catalytic response for various concentrations increases. In terms of heavy metal sensitivity, the modified electrode performs adequately [100–101].

Table 4 summarizes the LODs and correlation coefficients (R^2) of the BZV sensors for various analytes, including biomolecules, chemical drugs, and heavy metals. The results demonstrate the sensor's high sensitivity and specificity, with low LOD values ranging from 0.11×10^{-6} M for uric acid and ibuprofen to 0.58×10^{-6} M for paracetamol. The R^2 values, all above 0.87, confirm the strong linearity and accuracy of the sensor across different analyte concentrations.

This exceptional performance is attributed to the unique structural and electrochemical properties of BZV, which enable efficient electron transfer and strong interactions with

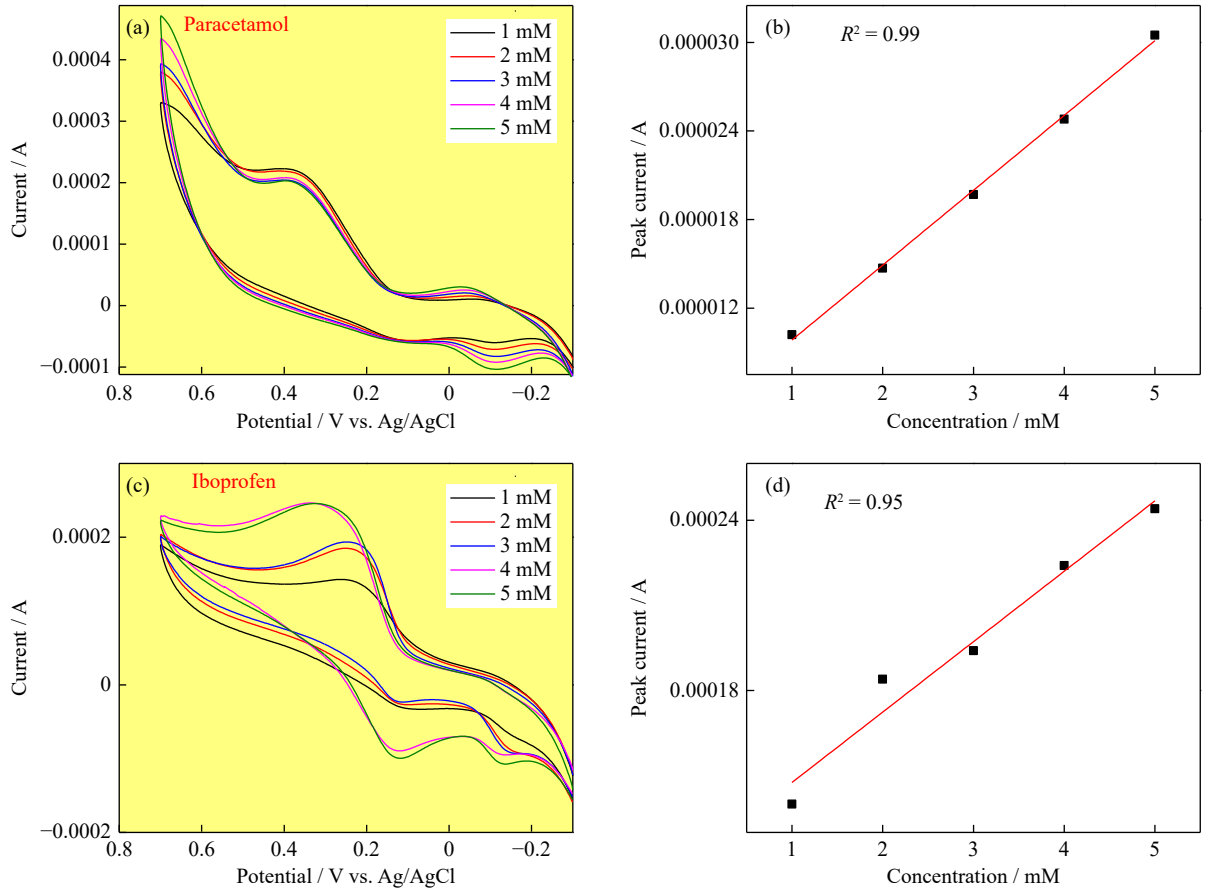

Fig. 15. Electrochemical sensing performance for paracetamol and ibuprofen: curves of the sensor in the presence of (a) paracetamol and (c) ibuprofen at varying concentrations; calibration plots of the oxidation peak current versus concentration derived from the CVs for (b) paracetamol and (d) ibuprofen.

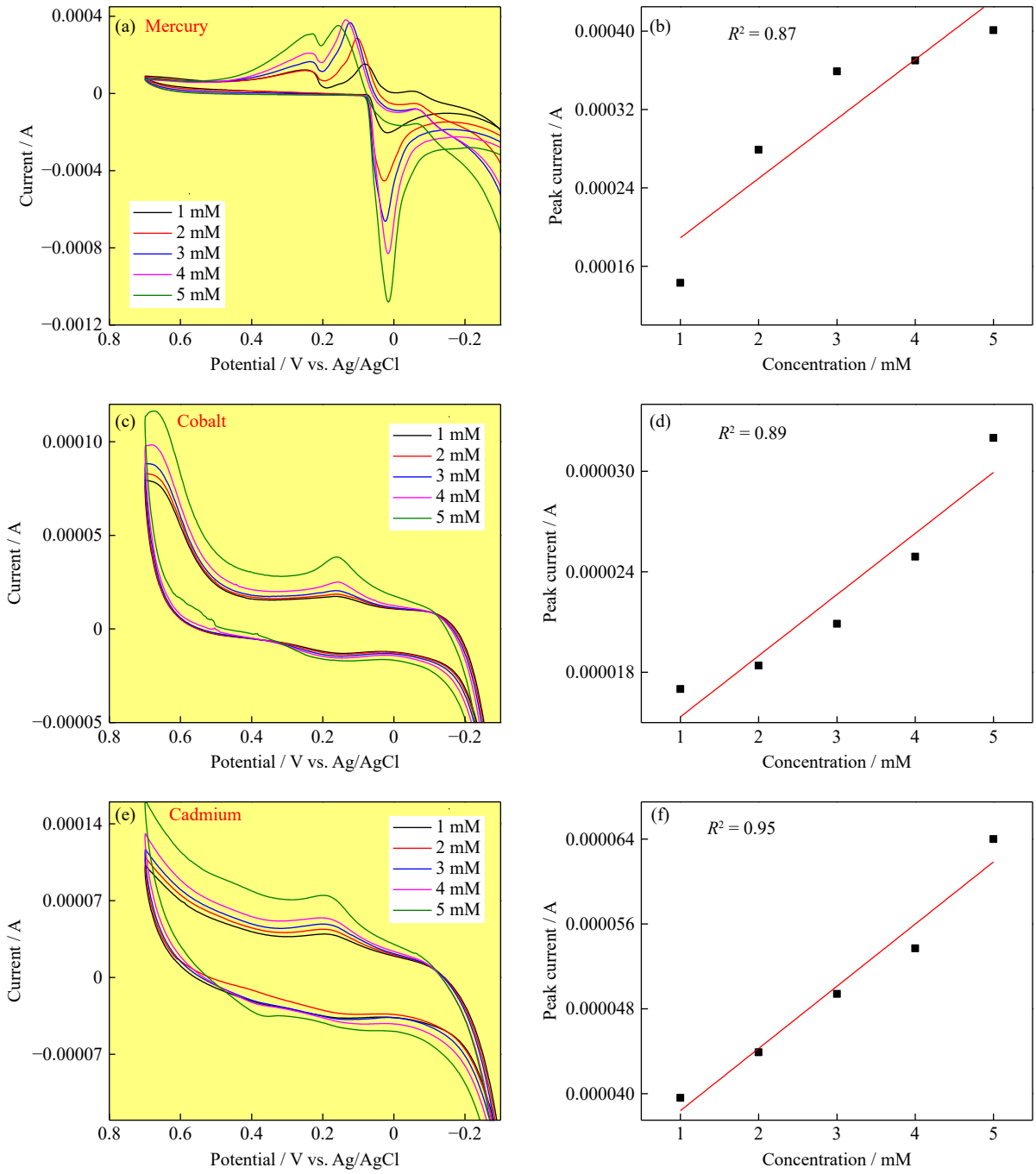

Fig. 16. Electrochemical sensing performance for mercury, cobalt, and cadmium: CV curves of the sensor in the presence of (a) mercury, (c) cobalt, and (e) cadium at varying concentrations; calibration plots of the oxidation peak current versus concentration derived from the CVs for (b) mercury, (d) cobalt, and (f) cadium.

target molecules. These findings establish BZV as a versatile sensing material suitable for the detection of critical biomolecules such as UA and AA, pharmaceuticals such as paracetamol and ibuprofen, and environmental pollutants such as mercury, cobalt, and cadmium. Its broad applicability and high sensitivity highlight its potential use in biomedical diagnostics and environmental monitoring.

8. Conclusion

The multifunctional characteristics of $BaZnV_2O_7$ nanoparticles were examined in this study, with particular attention paid to their photocatalytic activity, supercapacitor performance, and sensing abilities. Thorough structural and morphological characterization was performed using XRD, FTIR, UV-DRS, SEM, and EDAX. The BZV NPs have an energy bandgap of 5.28 eV, as shown by UV-DRS, and a crystallite size of 40.3 nm was determined by XRD. SEM shows an egg-like shape, EDAX analyses the elemental composition, and FTIR spectrum verifies the presence of functional groups. Under UV light, BZV NPs degraded AB-52 dye by 80.4%, according to the efficiency of photocatalytic experiments conducted at different pH levels, catalyst dosages, and dye dosages. An investigation using CV re-

vealed a high specific capacitance of 714.15 $F \cdot g^{-1}$ in a 1 M KCl electrolyte at a scan rate of 5 $mV \cdot s^{-1}$. With a specific capacitance of 857.4 $F \cdot g^{-1}$, GCD tests conducted 1000 cycles demonstrated exceptional cyclic stability and energy storage capacity. Furthermore, there are notable sensing properties. A new BZV electrochemical sensor was developed that demonstrated excellent stability and precision. It is capable of efficiently detecting heavy metals such as mercury, cobalt, and cadmium; chemical drugs such as ibuprofen and paracetamol; and biomolecules such as UA acid and AA. These findings highlight the versatility of BZVs in energy storage and environmental monitoring applications.

Acknowledgements

Abdullah N. Alodhayb acknowledges the fund provided by the Ongoing Research Funding program-Research Chairs (No. ORF-RC-2025-1609), King Saud University, Riyadh, Saudi Arabia.

Conflict of Interest

The authors have no competing interests to declare that are relevant to the content of this article.

References

[1] B.B. Zhu, J. Zhou, L.B. Ni, and G.W. Diao, Rapid removal of tetracycline by g-C_3N_4/high elastic graphene sponge via synergy effect of adsorption and photocatalysis under visible light, *Solid State Sci.*, 139(2023), art. No. 107158.

[2] L. Yang, R.J. Ding, C.S. Hong, and W.C. Zhu, Synthesis, optical and photocatalysis property of ZnO: Tb nanoparticles, *Solid State Sci.*, 131(2022), art. No. 106957.

[3] P. Dhiman, M. Patial, A. Kumar, *et al*., Environmental friendly and robust $Mg_{0.5-x}Cu_xZn_{0.5}Fe_2O_4$ spinel nanoparticles for visible light driven degradation of Carbamazepine: Band shift driven by dopants, *Mater. Lett.*, 284(2021), art. No. 129005.

[4] M. Prakash, H.P. Kavitha, S. Abinaya, J.P. Vennila, and D. Lohita, Green synthesis of bismuth based nanoparticles and its applications - A review, *Sustain. Chem. Pharm.*, 25(2022), art. No. 100547.

[5] J. Cevallos-Mendoza, C.G. Amorim, J.M. Rodríguez-Díaz, and M. da C.B.S.M. Montenegro, Removal of contaminants from water by membrane filtration: A review, *Membranes*, 12(2022), No. 6, art. No. 570.

[6] A. Saravanan, P.S. Kumar, D.N. Vo, *et al*., Photocatalysis for removal of environmental pollutants and fuel production: A review, *Environ. Chem. Lett.*, 19(2021), No. 1, p. 441.

[7] A. Kumar, G. Sharma, M. Naushad, *et al*., Bio-inspired and biomaterials-based hybrid photocatalysts for environmental detoxification: A review, *Chem. Eng. J.*, 382(2020), art. No. 122937.

[8] M. Aqeel, M. Rashid, M. Ikram, *et al*., Photocatalytic, dye degradation, and bactericidal behavior of Cu-doped ZnO nanorods and their molecular docking analysis, *Dalton Trans.*, 49 (2020), No. 24, p. 8314.

[9] K. Subramanyam, N. Sreelekha, D.A. Reddy, *et al*., Influence of transition metals co-doping on CeO_2 magnetic and photocatalytic activities, *Ceram. Int.*, 46(2020), No. 4, p. 5086.

[10] B. Biswas, M.F. Ahmed, M.L. Rahman, J. Khanam, M.H.R. Bhuiyan, and N. Sharmin, Investigation of structural, optical, and magnetic properties of $NiFe_2O_4$ for efficient photocatalytic degradation of organic pollutants through photo Fenton reactions, *Heliyon*, 10(2024), No. 17, art. No. e37199.

[11] A. Nazir, S. Alam, N. Alwadai, *et al*., Green synthesis of copper nanoparticles using Citrullus colocynthis leaves extract: Photocatalytic, antimicrobial and antioxidant studies, *Z. Phys. Chem.*, 237(2023), No. 11, p. 1733.

[12] B. Murugan, M.Z. Rahman, I. Fatimah, *et al*., Green synthesis of CuO nanoparticles for biological applications, *Inorg. Chem. Commun.*, 155(2023), art. No. 111088.

[13] S. Noreen, S. Ismail, S.M. Ibrahim, *et al*., ZnO, CuO and Fe_2O_3 green synthesis for the adsorptive removal of direct golden yellow dye adsorption: Kinetics, equilibrium and thermodynamics studies, *Z. Phys. Chem.*, 235(2021), No. 8, p. 1055.

[14] H. Arif, M. Yasir, F. Ali, *et al*., Photocatalytic degradation of atrazine and abamectin using Chenopodium album leaves extract mediated copper oxide nanoparticles, *Z. Phys. Chem.*, 237(2023), No. 6, p. 689.

[15] F. El-Sayed, M.S.A. Hussien, M.I. Mohammed, *et al*., The photocatalytic performance of Nd_2O_3 doped CuO nanoparticles with enhanced methylene blue degradation: Synthesis, characterization and comparative study, *Nanomaterials*, 12(2022), No. 7, art. No. 1060.

[16] S.T. Fardood, F. Moradnia, F.Y. Zare, *et al*., Green synthesis and characterization of α-Mn_2O_3 nanoparticles for antibacterial activity and efficient visible-light photocatalysis, *Sci. Rep.*, 14(2024), No. 1, art. No. 6755.

[17] H. Saha, A. Dastider, M.J.F. Anik, *et al*., Photocatalytic performance of CuO NPs: An experimental approach for process parameter optimization for Rh B dye, *Results Mater.*, 24(2024), art. No. 100614.

[18] M.E. Abo Elnaga, A.M. Abuelftooh, F.A. Taher, and S.G. Mohamed, Boosting supercapacitor performance: Sb_2O_3 nanoblocks on rGO sheets for enhanced energy storage, *Solid State Sci.*, 156(2024), art. No. 107655.

[19] C.R. Ravi kumar, P. Kotteeswaran, V.B. Raju, *et al*., Influence of zinc additive and pH on the electrochemical activities of β-nickel hydroxide materials and its applications in secondary batteries, *J. Energy Storage*, 9(2017), p. 12.

[20] V.V. Deshmukh, H.V. Harini, H.P. Nagaswarupa, R. Naik, and C.R. Ravikumar, Development of novel Co^{3+} doped $LaMnO_3$ perovskite electrodes for supercapacitors and sensors: Mechanism of electrochemical energy storage and oxygen intercalation, *J. Energy Storage*, 68(2023), art. No. 107805.

[21] R.T. Yadlapalli, R.R. Alla, R. Kandipati, and A. Kotapati, Super capacitors for energy storage: Progress, applications and challenges, *J. Energy Storage*, 49(2022), art. No. 104194.

[22] T. Ramachandran, S.S. Sana, K.D. Kumar, Y.A. Kumar, H.H. Hegazy, and S.C. Kim, Asymmetric supercapacitors: Unlocking the energy storage revolution, *J. Energy Storage*, 73(2023), art. No. 109096.

[23] B. Kalidasan, A.K. Pandey, R. Saidur, and V.V. Tyagi, Energizing organic phase change materials using silver nanoparticles for thermal energy storage, *J. Energy Storage*, 58(2023), art. No. 106361.

[24] S. Ahmad, S. Gouadria, K. Jabbour, *et al*., Iron doped $Gd_2Zr_2O_7$ hierarchical nanoflakes arrays as robust electrodes materials for energy storage application, *J. Energy Storage*, 60(2023), art. No. 106687.

[25] R.P. Kumar and G. Karthikeyan, A multi-objective optimization solution for distributed generation energy management in microgrids with hybrid energy sources and battery storage system, *J. Energy Storage*, 75(2024), art. No. 109702.

[26] L.N. Ramavathu and B. Tumma, Synthesis and characterization of zinc vanadate nanostructures for supercapacitor applications, *Trends Sci.*, 19(2022), No. 17, art. No. 5763.

[27] A.Z. AL Shaqsi, K. Sopian, and A. Al-Hinai, Review of energy storage services, applications, limitations, and benefits, *Energy Rep.*, 6(2020), p. 288.
[28] M.I.A.A. Maksoud, R.A. Fahim, A.E. Shalan, *et al.*, Advanced materials and technologies for supercapacitors used in energy conversion and storage: A review, *Environ. Chem. Lett.*, 19(2021), No. 1, p. 375.
[29] V.V. Deshmukh, H.V. Harini, R. Naik, *et al.*, Enhanced multifunctional properties of lanthanum-doped barium ferrite nanoparticles synthesized via sol–gel assisted hydrothermal method, *J. Energy Storage*, 82(2024), art. No. 110559.
[30] H. Alhumade, A.G. Olabi, H. Rezk, P.A. Shinde, and M. Ali Abdelkareem, Marine predators optimization and ANFIS as an effective tools for maximization of specific capacity of G-NiO electrode for electrochemical energy storage, *Ain Shams Eng. J.*, 14(2023), No. 10, art. No. 102210.
[31] A. Numan, Y.Q. Zhan, M. Khalid, and M. Hatamvand, Introduction to Supercapattery, [in] N. Arshid, M. Khalid, and A.N. Grace, eds., *Advances in Supercapacitor and Supercapattery*. Elsevier, 2021, p. 45.
[32] L. Naik Ramavathu, S. Rao Harapanahalli, N. Pernapati, and B. Tumma, Synthesis and characterization of Nickel Metavanadate ($Ni_3V_2O_8$)-application as photocatalyst and supercapacitor, *Int. J. Nano Dimens.*, 12(2021), No. 4. p.411.
[33] K. Yang, S.S. Cheng, Z.Q. Yao, S.J. Li, and Y.T. Yang, Dumbbell shaped nanocomposite Co_3O_4/CeO_2 derived from metal-organic frameworks (MOFs) as an excellent non-enzymatic glucose sensor, *Solid State Sci.*, 150(2024), art. No. 107498.
[34] S.J. Kim, Y. Cho, C. Lee, M.H. Kim, and Y. Lee, Real-time direct electrochemical sensing of ascorbic acid over rat liver tissues using RuO_2 nanowires on electrospun TiO_2 nanofibers, *Biosens. Bioelectron.*, 77(2016), p. 1144.
[35] B. Kaur, R. Srivastava, and B. Satpati, Ultratrace detection of toxic heavy metal ions found in water bodies using hydroxyapatite supported nanocrystalline ZSM-5 modified electrodes, *New J. Chem.*, 39(2015), No. 7, p. 5137.
[36] M.B. Gumpu, N. Nesakumar, S. Sethuraman, U.M. Krishnan, and J.B.B. Rayappan, Development of electrochemical biosensor with ceria-PANI core–shell nano-interface for the detection of histamine, *Sens. Actuators B.*, 199(2014), p. 330.
[37] W.H. Gao, Y.S. Chen, J. Xi, *et al.*, A novel electrochemiluminescence ethanol biosensor based on tris(2, 2'–bipyridine) ruthenium (II) and alcohol dehydrogenase immobilized in graphene/bovine serum albumin composite film, *Biosens. Bioelectron.*, 41(2013), p. 776.
[38] J.Y. Kim, K.H. Kim, S.B. Yoon, H.K. Kim, S.H. Park, and K.B. Kim, *In situ* chemical synthesis of ruthenium oxide/reduced graphene oxide nanocomposites for electrochemical capacitor applications, *Nanoscale*, 5(2013), No. 15, p. 6804.
[39] L.L. Wang, T.M. Yao, S. Shi, Y.L. Cao, and W.L. Sun, A label-free fluorescent probe for Hg^{2+} and biothiols based on graphene oxide and Ru-complex, *Sci. Rep.*, 4(2014), art. No. 5320.
[40] C. Pérez-Ràfols, N. Serrano, J.M. Díaz-Cruz, C. Ariño, and M. Esteban, Glutathione modified screen-printed carbon nanofiber electrode for the voltammetric determination of metal ions in natural samples, *Talanta*, 155(2016), p. 8.
[41] D.M. Tejashwini, H.V. Harini, H.P. Nagaswarupa, R. Naik, V.V. Deshmukh, and N. Basavaraju, An in-depth exploration of eco-friendly synthesis methods for metal oxide nanoparticles and their role in photocatalysis for industrial dye degradation, *Chem. Phys. Impact*, 7(2023), art. No. 100355.
[42] M.R. Anil Kumar, B. Abebe, H.P. Nagaswarupa, H.C. Ananda Murthy, C.R. Ravikumar, and F.K. Sabir, Enhanced photocatalytic and electrochemical performance of TiO_2–Fe_2O_3 nanocomposite: Its applications in dye decolorization and as supercapacitors, *Sci. Rep.*, 10(2020), No. 1, art. No. 1249.
[43] J.W. Li, K. McColl, X.K. Lu, *et al.*, Multi-scale investigations of δ-$Ni_{0.25}V_2O_5{\cdot}nH_2O$ cathode materials in aqueous zinc-ion batteries, *Adv. Energy Mater.*, 10(2020), No. 15, art. No. 2000058.
[44] Y.F. Zhang, J.Q. Zheng, Y.F. Zhao, T. Hu, Z.M. Gao, and C.G. Meng, Fabrication of V_2O_5 with various morphologies for high-performance electrochemical capacitor, *Appl. Surf. Sci.*, 377(2016), p. 385.
[45] B. Hadrane, P. Deniard, N. Gautier, M. Paris, C. Payen, and R. Dessapt, Micro- and nanostructured layered-kagome zinc orthovanadate $BaZn_3(VO_4)_2(OH)_2$, *Dalton Trans.*, 52(2023), No. 45, p. 16927.
[46] L.X. Zhang, G.N. Li, Y.Y. Yin, *et al.*, $Zn_3(VO_4)_2$-decoration induced acetone sensing improvement of defective ZnO nanosheet spheres, *Sens. Actuators B*, 325(2020), art. No. 128805.
[47] V.R. Bandi, B.K. Grandhe, M. Jayasimhadri, *et al.*, Photoluminescence and structural properties of $Ca_3Y(VO_4)_3$: RE^{3+} (= Sm^{3+}, Ho^{3+} and Tm^{3+}) powder phosphors for tri-colors, *J. Cryst. Growth*, 326(2011), No. 1, p. 120.
[48] V. Chauhan,, P. Deshmukh, S. Satapathy, and P.C. Pandey, Greenish-yellow emission from rare-earth free Li^+ doped zinc vanadate phosphor. *Results Phys.*, 39(2022), art. No. 105689.
[49] A. Suguna, S. Prabhu, M. Selvaraj, *et al.*, Annealing effect on photocatalytic activity of ZnO nanostructures for organic dye degradation, *J. Mater. Sci. Mater. Electron.*, 33(2022), No. 11, p. 8868.
[50] R. enukadevi, R. Sundaram, and K. Kasinathan. Barium oxide nanoparticles with robust catalytic, photocatalytic and humidity sensing properties. *J. Nanostruct.*, 10(2020), No. 1, P. 167.
[51] L.Z. Pei, N. Lin, T. Wei, H.D. Liu, and H.Y. Yu, Zinc vanadate nanorods and their visible light photocatalytic activity, *J. Alloys Compd.*, 631(2015), p. 90.
[52] T.A. Vu, C.D. Dao, T.T.T. Hoang, *et al.*, Synthesis of novel silver vanadates with high photocatalytic and antibacterial activities, *Mater. Lett.*, 123(2014), p. 176.
[53] M.A.S. Amulya, H.P. Nagaswarupa, M.R.A. Kumar, C.R. Ravikumar, and K.B. Kusuma, Sonochemical synthesis of Mn-Fe_2O_4 nanoparticles and their electrochemical and photocatalytic properties, *J. Phys. Chem. Solids*, 148(2021), art. No. 109661.
[54] Y.H. Chiu, T.F.M. Chang, C.Y. Chen, M. Sone, and Y.J. Hsu, Mechanistic insights into photodegradation of organic dyes using heterostructure photocatalysts, *Catalysts*, 9(2019), No. 5, art. No. 430.
[55] A. Ilyas, K. Rafiq, M.Z. Abid, A. Rauf, and E. Hussain, Growth of villi-microstructured bismuth vanadate (Vm–$BiVO_4$) for photocatalytic degradation of crystal violet dye, *RSC Adv.*, 13(2023), No. 4, p. 2379.
[56] X.N. Wang, F.L. Wang, Y.H. Sang, and H. Liu, Full-spectrum solar-light-activated photocatalysts for light–chemical energy conversion, *Adv. Energy Mater.*, 7(2017), No. 23, art. No. 1700473.
[57] S. Rojas-Carbonell, K. Artyushkova, A. Serov, C. Santoro, I. Matanovic, and P. Atanassov, Effect of pH on the activity of platinum group metal-free catalysts in oxygen reduction reaction, *ACS Catal.*, 8(2018), No. 4, p. 3041.
[58] C.L. Jiang, H. Wang, Y.Q. Wang, and H.B. Ji, All solid-state Z-scheme $CeO_2/ZnIn_2S_4$ hybrid for the photocatalytic selective oxidation of aromatic alcohols coupled with hydrogen evolution, *Appl. Catal. B: Environ.*, 277(2020), art. No. 119235.
[59] G.A. Ismail and H. Sakai, pH-dependent dye protonation and the effect of iron on dye degradation during Fenton-based processes, *Ozone Sci. Eng.*, 46(2024), No. 4, p. 294.
[60] I. Mahboob, I. Shafiq, S. Shafique, *et al.*, Effect of active species scavengers in photocatalytic desulfurization of hydro-

cracker diesel using mesoporous Ag_3VO_4. *Chem. Eng. J.*, 441(2022), art. No. 136063.

[61] A. Trenczek-Zajac, M. Synowiec, K. Zakrzewska, *et al*., Scavenger-supported photocatalytic evidence of an extended type I electronic structure of the TiO_2@Fe_2O_3 interface, *ACS Appl. Mater. Interfaces*, 14(2022), No. 33, p. 38255.

[62] Z. Sabouri, A. Akbari, H.A. Hosseini, and M. Darroudi, Facile green synthesis of NiO nanoparticles and investigation of dye degradation and cytotoxicity effects, *J. Mol. Struct.*, 1173(2018), p. 931.

[63] M.S. Sunil Kumar, T.L. Soundarya, Udayabhanu, *et al*., Multifunctional applications of Nickel oxide (NiO) nanoparticles synthesized by facile green combustion method using Limonia acidissima natural fruit juice, *Inorg. Chim. Acta*, 515(2021), art. No. 120059.

[64] Z. Sabouri, A. Akbari, H. Ali Hosseini, M. Khatami, and M. Darroudi, Egg white-mediated green synthesis of NiO nanoparticles and study of their cytotoxicity and photocatalytic activity, *Polyhedron*, 178(2020), art. No. 114351.

[65] M.R. Anil Kumar, B. Mahendra, H.P. Nagaswarupa, B.S. Surendra, C.R. Ravikumar, and K. Shetty, Photocatalytic studies of MgO nano powder; synthesized by green mediated route, *Mater. Today Proc.*, 5(2018), No. 10, p. 22221.

[66] B. Khatri, I.B. Bamma, and A. Rajbhandari, Bismuth vanadate, an agile photocatalyst for the degradation of malachite green dye, *Int. J. Chem. stud.*, 7(2019), p. 595.

[67] Y.M. Hunge, A. Uchida, Y. Tominaga, *et al*., Visible light-assisted photocatalysis using spherical-shaped $BiVO_4$ photocatalyst, *Catalysts*, 11(2021), No. 4, art. No. 460.

[68] I.J. Radhi, A.M.A. Hindawi, H.Q. AL-Masoud, N.A. Hamza, Z.M.A. Al-Aama, and M.A. Hasan, V_2O_5/ZnO/Pd nanocomposites: preparation, characterization and studying the photocatalytic activity against malachite green, *Chem. Rev. Lett.*, 8(2025), No. 5, p.1061.

[69] Y. Lu, Y.S. Luo, H.M. Xiao, and S.Y. Fu, Novel core–shell structured $BiVO_4$ hollow spheres with an ultra-high surface area as visible-light-driven catalyst, *CrystEngComm*, 16(2014), No. 27, p. 6059.

[70] S.H. Abed and A.H. Reshak, Illuminating the power of V_2O_5 nanoparticles: Efficient photocatalytic degradation of organic dyes under visible light, *J. Fluoresc.*, 35(2025), No. 6, p. 4335.

[71] A.A. Yadav, Y.M. Hunge, S.W. Kang, A. Fujishima, and C. Terashima, Enhanced photocatalytic degradation activity using the V_2O_5/RGO composite, *Nanomaterials*, 13(2023), No. 2, art. No. 338.

[72] N. Sarengan, S. Salaeh, S. Sagadevan, S.S. Imam, C. Kusumawardani, and N.H.M. Kaus, Exploring the n–p type zinc oxide/copper oxide nanocomposite under Xenon light irradiation with enhanced photocatalytic activities for norfloxacin and methyl orange, *J. Mater. Sci. Mater. Electron.*, 35(2024), No. 32, art. No. 2054.

[73] R.A. Alkhadry, I.S. Yahia, S.A. Elfeky, *et al*., Novel synthesized V_2O_5-doped PMMA nanocomposite films for effective photocatalytic removal of methylene blue from water. *J. Sol-Gel Sci. Technol*., (2025), p.1.

[74] F. Mazloom, M. Ghiyasiyan-Arani, R. Monsef, and M. Salavati-Niasari, Photocatalytic degradation of diverse organic dyes by sol–gel synthesized $Cd_2V_2O_7$ nanostructures, *J. Mater. Sci. Mater. Electron.*, 29(2018), No. 21, p. 18120.

[75] T. Du, M. Cui, Y. Chao, *et al*., Preparation and photocatalytic properties of highly dispersed samarium vanadate nanoparticles supported on H-mordenite composites by template-free method, *J. Photochem. Photobiol. A*, 433(2022), art. No. 114207.

[76] P.J. Mafa, M.E. Malefane, A.O. Idris, *et al*., Cobalt oxide/copper bismuth oxide/samarium vanadate (Co_3O_4/$CuBi_2O_4$/$SmVO_4$) dual Z-scheme heterostructured photocatalyst with high charge-transfer efficiency: Enhanced carbamazepine degradation under visible light irradiation, *J. Colloid Interface Sci.*, 603(2021), p. 666.

[77] V. Dubey, K.D. Parikh, R.J. Jadav, *et al*., Eco-Friendly Fabrication of $Cr_2V_4O_{13}$ Nanoparticles: A Promising Material for Photocatalysis, Electrochemical Sensing, and Supercapacitor Applications. *J. Cluster Sci*. 36(2025), No.1, art. No. 9.

[78] H.J. Huang, D.Z. Li, Q. Lin, *et al*., Efficient degradation of benzene over $LaVO_4$/TiO_2 nanocrystalline heterojunction photocatalyst under visible light irradiation, *Environ. Sci. Technol.*, 43(2009), No. 11, p. 4164.

[79] M. Mastragostino and F. Soavi, Pseudocapacitive and ion-insertion materials: A bridge between energy storage, electronics and neuromorphic computing, *ChemElectroChem*, 8(2021), No. 14, p. 2630.

[80] S. Munir, I. Shakir, M. Anwar, *et al*., An insight into synergistic effect of polyaniline and noble metal (Ag) on vanadium pentoxide nanorods for enhanced energe storage performance, *J. Indian Chem. Soc.*, 101(2024), No. 11, art. No. 101440.

[81] B.C. Sekhar, A. Soliman, M. Arsalan, and E.H. Alsharaeh, A 2D hybrid nanocomposite: A promising anode material for lithium-ion batteries at high temperature, *Nanoscale Adv.*, 6(2024), No. 22, p. 5612.

[82] E.J. Nixon, A. Jayapaul, R.J. Chung, S. Rajkumar, and J.P. Merlin, Antimony vanadate spheres: Synthesis, characterizations, and use as positive electrode in asymmetric supercapacitor systems, *J. Electroanal. Chem.*, 953(2024), art. No. 118014.

[83] S. Ezhil Arasi, R. Ranjithkumar, P. Devendran, M. Krishnakumar, and A. Arivarasan, Investigation on electrochemical behaviour of manganese vanadate nanopebbles as potential electrode material for supercapacitors, *J. Alloy. Compd.*, 857(2021), art. No. 157628.

[84] K. Venkatesh, B. Arumugam, S.M. Chen, *et al*., Synthesis and characterization of manganese vanadate nanopebbles: As energetic electrode material for trichlorophenol detection and supercapacitor applications, *J. Energy Storage*, 59(2023), art. No. 106385.

[85] S. Ezhil Arasi, P. Devendran, R. Ranjithkumar, S. Arunpandiyan, and A. Arivarasan, Electrochemical property analysis of zinc vanadate nanostructure for efficient supercapacitors, *Mater. Sci. Semicond. Process.*, 106(2020), art. No. 104785.

[86] B. Muthukumar, A. Surulinathan, H. Gubendran, *et al*., Synthesis, structural and electrochemical investigations of reduced graphene oxide loaded zinc vanadate nanoparticles for high performance supercapacitors, *J. Energy Storage*, 74(2023), art. No. 109331.

[87] S. Ishwarya, H.P. Nagaswarupa, R. Naik, *et al*., Multifunctional, energy and environmental applications of calcium magnesium vanadate ($Ca_5Mg_4V_6O_{24}$) nanoparticles synthesized by solution combustion, *J. Appl. Electrochem.*, 55(2025), No. 2, p. 357.

[88] Y. He, H.Y. Xu, F.L. Liu, *et al*., De-ammonium $Ba_{0.18}V_2O_{4.95}$/$NH_4V_4O_{10}$ film electrodes as high-performance cathode materials for magnesium-ion batteries, *Langmuir*, 39(2023), No. 18, p. 6580.

[89] M.W. Alam, Green combustion synthesis of copper magnesium vanadate (CuMgV) NPs using neem extract: Its photocatalytic and supercapacitor applications, *Appl. Organomet. Chem.*, 39(2025), No. 3, art. No. e7899.

[90] S. Ishwarya, H.P. Nagaswarupa, R. Naik, and N. Basavaraju, Multifunctional applications of novel copper magnesium vanadate nanoparticles: Photocatalytic dye degradation and electrochemical properties, *Microchem. J.*, 206(2024), art. No. 111489.

[91] A. Vedpathak, T. Shinde, M.A. Desai, *et al*., One-dimensional layered sodium vanadate nanobelts: A potential aspirant for

high-performance supercapacitor applications, *ACS Appl. Energy Mater.*, 6(2023), No. 9, p. 4693.

[92] R. Lakshmana Naik, T. Bala Narsaiah, P. Justin, *et al*., Hydrothermally synthesized cobalt vanadate nanoparticles for photocatalytic degradation of Fast Orange Red dye and supercapacitor applications, *Mater. Sci. Eng. B*, 298(2023), art. No. 116861.

[93] A. Kumar, V.N. Thakur, A. Kumar, V. Singh, A. Dhaka, and R.S. Dhaka, Dielectric behavior and impedance spectroscopy of Niobium substituted Lanthanum based orthovanadates at high temperatures, *Ceram. Int.*, 50(2024), No. 4, p. 6735.

[94] S.B. Aziz, R.T. Abdulwahid, P.A. Mohammed, *et al*., Steps towards the ideal CV and GCD results with biodegradable polymer electrolytes: Plasticized MC based green electrolyte for EDLC application, *J. Energy Storage*, 76(2024), art. No. 109730.

[95] Y.L. Zhang, X. Li, Z.H. Li, and F.Q. Yang, Evaluation of electrochemical performance of supercapacitors from equivalent circuits through cyclic voltammetry and galvanostatic charge/discharge, *J. Energy Storage*, 86(2024), art. No. 111122.

[96] S.M. Babulal, C. Koventhan, S.M. Chen, and W. Hung, Construction of sphere like samarium vanadate nanoparticles anchored graphene nanosheets for enhanced electrochemical detection of nitrofurantoin in biological fluids, *Composites Part B*, 237(2022), art. No. 109847.

[97] G. Kesavan, M. Pichumani, S.M. Chen, and C.J. Wu, Hydrothermal synthesis of iron vanadate nanoparticles for voltammetric detection of antipsychotic drug thioridazine, *J. Alloy. Compd.*, 885(2021), art. No. 160880.

[98] V. Sivakumar, R. Suresh, K. Giribabu, *et al*., Copper vanadate nanoparticles: Synthesis, characterization and its electrochemical sensing property, *J. Mater. Sci. Mater. Electron.*, 25(2014), No. 3, p. 1485.

[99] Y. Liu, X. Xu, C.R. Ma, F. Zhao, and K. Chen, Morphology effect of bismuth vanadate on electrochemical sensing for the detection of paracetamol, *Nanomaterials*, 12(2022), No. 7, art. No. 1173.

[100] R.T. Yogeeshwari, R.H. Krishna, P.S. Adarakatti, and S. Ashoka, Ultra-trace detection of toxic heavy metal ions using graphitic carbon functionalized Co_3O_4 modified screen-printed electrode, *Carbon Lett.*, 32(2022), No. 1, p. 181.

[101] A. Toghan, M. Abd-Elsabour, and A.M. Abo-Bakr, A novel electrochemical sensor based on EDTA–NQS/GC for simultaneous determination of heavy metals, *Sens. Actuator A*, 322(2021), art. No. 112603.